

# EquiReg: Equivariance Regularized Diffusion for Inverse Problems

Bahareh Tolooshams\*, Aditi Chandrashekar\*, Rayhan Zirvi\*  
 Abbas Mammadov, Jiachen Yao, Chuwei Wang, Anima Anandkumar  
 Computing and Mathematical Sciences, California Institute of Technology  
 \*Co-first authors

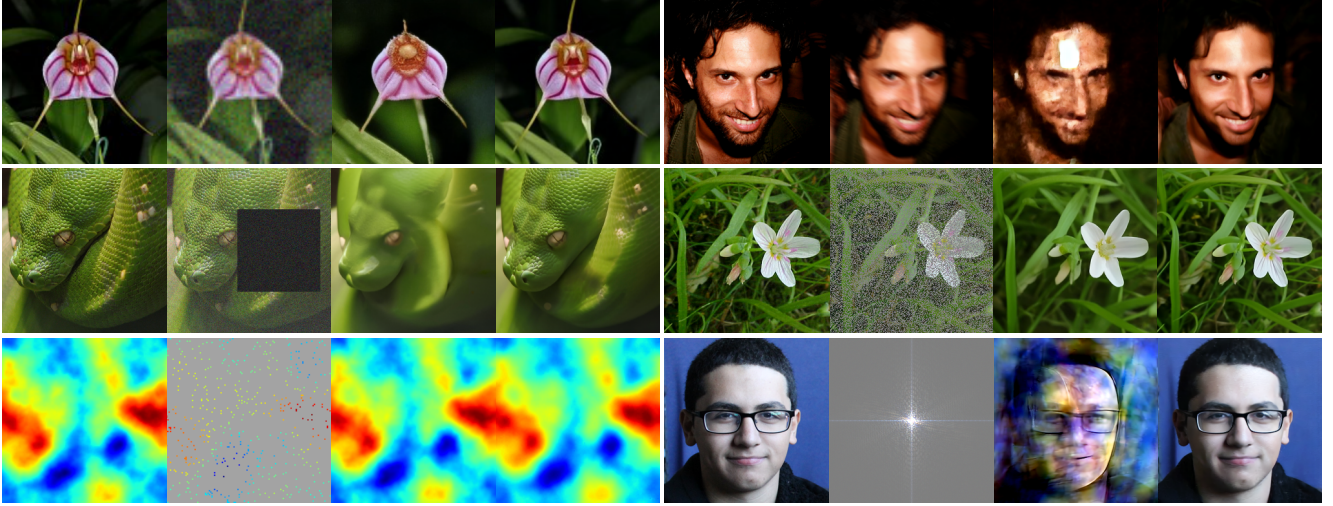


Figure 1: **Ground truth, measurement, baseline, and reconstruction.** R1 (left-to-right): super-resolution and motion deblur. R2: box and random inpainting. R3: PDE solving and phase retrieval.

## Abstract

Diffusion models represent the state-of-the-art for solving inverse problems such as image restoration tasks. In the Bayesian framework, diffusion-based inverse solvers incorporate a likelihood term to guide the prior sampling process, generating data consistent with the posterior distribution. However, due to the intractability of the likelihood term, many current methods rely on isotropic Gaussian approximations, which lead to deviations from the data manifold and result in inconsistent, unstable reconstructions. We propose *Equivariance Regularized* (EquiReg) diffusion, a general framework for regularizing posterior sampling in diffusion-based inverse problem solvers. EquiReg enhances reconstructions by reweighting diffusion trajectories and penalizing those that deviate from the data manifold. We define a new distribution-dependent equivariance error, empirically identify functions that exhibit low error for on-manifold samples and higher error for off-manifold samples, and leverage these functions to regularize the diffusion sampling process. When applied to a variety of solvers, EquiReg outperforms state-of-the-art diffusion models in both linear and nonlinear image restoration tasks, as well as in reconstructing partial differential equations.

## 1 Introduction

Inverse problems consider the problem of recovering an unknown signal  $x^* \in \mathbb{R}^d$  from undersampled noisy measurements:

$$y = \mathcal{A}(x^*) + \nu \in \mathbb{R}^m, \quad (1)$$

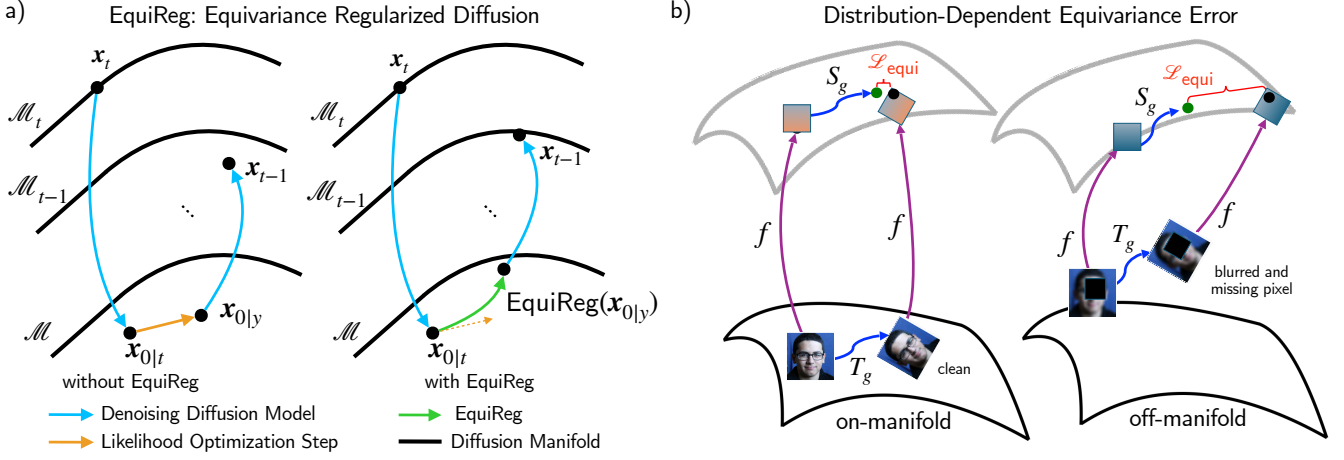


Figure 2: **Equivariance Regularized (EquiReg) diffusion for solving inverse problems.** a) EquiReg regularizes the posterior sampling trajectory, addressing the errors introduced due to the posterior mean expectation. b) The EquiReg loss function is lower for on- or near-manifold (clean) data and higher for off- or far-from-manifold (blurred and missing pixel) data.

where  $\mathcal{A}$  is a known measurement operator, and  $\nu$  is an unknown noise [1]. Inverse problems are widely applied and studied in science and engineering, including imaging science [2], medical imaging [3, 4], image restorations [5–8], computational neuroscience [9], seismology [10], radar imaging [11, 12], source separation [13–15], and astrophotography [16].

Inverse problems are ill-posed, i.e., the inversion process can have many solutions; hence, they require prior information about the desired solution [17]. Classical approaches use regularization techniques to improve the stability and offer uniqueness of the inversion, formulated as  $\min_{x \in \mathbb{R}^d} \|\mathbf{y} - \mathcal{A}(x)\|^2 + \mathcal{R}(x)$ , where the first term encapsulates the forward model error and  $\mathcal{R}$  is a function regularizing the solution. Bayesian inference formulates the inverse problem as finding  $x$  maximizing the *posterior distribution*  $p(x|\mathbf{y}) \propto p(\mathbf{y}|x)p(x)$  where  $p(\mathbf{y}|x)$  is the *likelihood* of the measurements given the signal, and  $p(x)$  is a *prior* characterizing the signal structure [18]. Sparsity [19–23], low-rank [24, 25], and total variation [26] are examples of hand-crafted regularizers, imposing a prior model.

This paper focuses on methods that leverage unconditionally pre-trained score-based generative diffusion models as learned priors [27–30]. These methods define a sequential noising process  $x_0 \sim p_{\text{data}} \rightarrow x_t \rightarrow x_T \sim p_T(x) \approx \mathcal{N}(\mathbf{0}, \mathbf{I})$  and a reverse denoising process parameterized by a neural network score  $\nabla_{x_t} \log p_t(x_t)$  [31, 30]. During sampling, these approaches incorporate gradient signals carrying likelihood-related information to solve inverse problems. Applications include image restoration [32–41], medical imaging [42–49], and solving partial differential equations (PDEs) [50–57].

Solving inverse problems with diffusion [32–49, 51, 52, 58, 59] requires computing the conditional score  $\nabla_{x_t} \log p_t(x_t|\mathbf{y})$ , decomposed into  $\nabla_{x_t} \log p_t(x_t) + \nabla_{x_t} \log p_t(\mathbf{y}|x_t)$ . This introduces challenges, as the likelihood score  $\nabla_{x_t} \log p_t(\mathbf{y}|x_t)$  is only computationally tractable when  $t = 0$ . To handle the intractable likelihood for  $t > 0$ , many state-of-the-art methods approximate the posterior  $p_t(x_0|x_t)$  with the

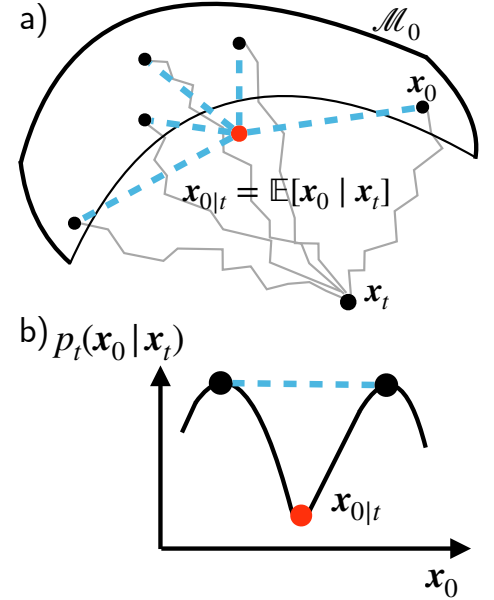


Figure 3: **Illustration of off-manifold posterior expectation.** a) Manifold interpretation. While samples from  $p(x_0|x_t)$  may lie on the manifold, their posterior expectation, being a linear combination, can fall off the manifold. b) Distribution interpretation. In a bimodal distribution, the posterior expectation lies in a low probability region.



40, 60], where the distribution expectation  $x_{0|t} := \mathbb{E}[x_0|x_t]$  is computed via Tweedie’s formula using the optimal denoising score  $s_\theta(x_t, t)$ .

This Gaussian approximation may be inaccurate (e.g., for a bimodal or a highly complex distribution). Moreover, this poor estimation can result in very high errors in likelihood score computation, especially when point estimations are employed as in DPS and PS�D [32, 38]. Conditional expectation, as in the posterior mean expectation, computes a linear combination of all possible  $x_0$ ; hence, from the manifold perspective, the posterior mean expectation may end up being located off-manifold (see Figure 3). The approximation error is further exacerbated when using latent diffusion models [61, 38], and can lead to artifacts in image restoration [32].

To address this error source, prior work explores projection-based methods that project either the diffusion state [62] or the measurement gradient [33, 41] onto the data manifold. However, each has limitations: [62] relies on a learned projector at every step, leading to accumulated errors; [33] assumes a noiseless setting; [41] uses SVD, which may not generalize beyond natural images. Other works incorporate higher-order information [63–65], but most large-scale applications still adopt the isotropic Gaussian approximation for its efficiency, scalability, and simplicity [40].

**Our contributions.** We propose *Equivariance Regularized* (EquiReg) diffusion, a symmetry-driven regularization framework for solving inverse problems with diffusion models (Figure 2).

- **Generalized regularization via Wasserstein gradient flow:** We reinterpret the reversed conditional diffusion as a Wasserstein-2 gradient flow minimizing a functional over sample trajectories. This framework suggests employing a regularizer that reweights and penalizes trajectories deviating from the data manifold. This addresses errors arising in the likelihood score due to poor approximations of the posterior  $p_t(x_0|x_t)$ , as well as prior score errors resulting from off-manifold trajectories. Unlike prior works, this approach provides a generalized regularization strategy over the entire reverse diffusion process. To realize such a regularizer, we seek an approach for manifold alignment via global properties of the data distribution. We take equivariance as one such global property that can enforce geometric symmetries.
- **EquiReg with distribution-dependent equivariance errors:** We propose a new class of regularizers grounded in distribution-dependent equivariance error, a formalism that quantifies how symmetry violations vary depending on whether samples lie on- or off-manifold. We introduce Manifold-Preferential Equivariant (MPE) functions, which exhibit low equivariance error on the support of the data manifold (in-distribution) and higher error off-manifold (out-of-distribution). Our proposed regularization, EquiReg, is based on this MPE property.
- **Identifying manifold-preferential equivariant functions:** We present two strategies for finding MPE functions: a) training induced, where equivariance emerges in encoder-decoder architectures trained with symmetry-preserving augmentations, and b) data inherent, where MPE arises from inherent data symmetries, commonly observed in physical systems.
- **Two practical equivariance regularizers:** We develop two flexible plug-and-play losses, Equi and EquiCon (Equi with an implicit manifold constraint), which can be integrated into a variety of pixel- and latent-space diffusion models to improve solving inverse problems. Both regularizations guide the sampling trajectory toward symmetry-preserving regions which often lie close to the data manifold, improving posterior sampling.
- **Improved image restoration performance:** We demonstrate that EquiReg significantly improves performance on linear and nonlinear image restoration tasks (Tables 1 to 3). For example, Equi-DPS improves the FID of DPS [32] by 59% on super-resolution ( $\times 4$ ). On motion deblur, EquiCon-ReSample improves the LPIPS of ReSample [37] by 51%. Moreover, EquiReg consistently shows improvement in performance across many noise levels (Figure 5).
- **Improved PDE reconstruction performance:** We show that EquiReg enhances performance on PDE solving tasks (Table 4). For instance, Equi-FunDPS reduces the relative  $\ell_2$  error of FunDPS [56, 57] from 17.16% to 15.91% on Helmholtz inverse problems and from 8.48% to 7.84% on Navier-Stokes inverse problems.

## 2 Related Works

**Diffusion models for generation.** Diffusion generative models [27, 28, 66, 67] are state-of-the-art in computer vision for image [68, 69] and video generation [61, 70–73], with score-based methods [30] being among the most widely used. Recent work has leveraged pre-trained diffusion models for text-guided image generation [74–78], while others, including variational approaches [79–81], have employed diffusion models to solve inverse problems by conditioning on measurements [32–49, 51, 52, 58, 59]. Another line of work uses text conditioning to improve inverse problem solutions [82]. The most widely adopted text-to-image diffusion models are latent diffusion models (LDMs) [61], which typically use classifier-free guidance [83]. Large-scale diffusion models for image [84, 85] and video generation [71] are also based on LDMs.

**Diffusion models for inverse problems.** Solving inverse problems with pre-trained diffusion models requires approximating the intractable likelihood score  $\nabla_{\mathbf{x}_t} \log p_t(\mathbf{y}|\mathbf{x}_t)$ . Diffusion-based inverse solvers differ in how they approximate the likelihood  $p_t(\mathbf{y}|\mathbf{x}_t)$  and integrate it with the sampling prior  $p_t(\mathbf{x}_t)$  [63]. To make the likelihood tractable, a common assumption is an isotropic Gaussian approximation of the posterior distribution  $p_t(\mathbf{x}_0|\mathbf{x}_t)$  [32, 86, 60, 38]. Prior work employs the empirical Bayes estimator (known as Tweedie’s formula) [87–89] to estimate the posterior expectation. Peng et al. [63] provides a unifying perspective on this approach and proposes a non-isotropic Gaussian approximation, aligning with other works using higher-order information [64, 65].

**Equivariant deep learning.** Equivariance is a strategy for incorporating symmetries into deep learning [90]. Prior work has applied it to graph networks [91], convolutional networks [92, 93], and Lie groups for modeling dynamical systems [94]. The extension of equivariance to probabilistic symmetries [95] has enabled the development of sample efficient diffusion models [96], with applications in molecular generation [97–100], autonomous driving [101], robotics [102], crystal structure prediction [103], and audio inverse problems [104].

Prior work has used equivariance as a data prior for solving inverse problems such as super-resolution and deblurring [105], either by training the inverter networks with pre-defined equivariance properties [106], or enforcing it on learned denoisers [107]. Their empirical benefits are supported by theoretical analysis in compressed sensing, showing that equivariance enables solving inverse problems with fewer measurements [108]. In diffusion models, equivariance guidance has been applied to improve temporal consistency in video generation [70], and to break symmetry for generation [109]. These prior studies focus on denoising scores for generation, while we use equivariance to correct likelihood-induced errors in inverse problems and restoration.

## 3 Preliminaries

**Diffusion models.** Diffusion models [27–29, 66, 67] generate data via a reverse noising process. The forward noising process transforms the data sample  $\mathbf{x}_0 \sim p_{\text{data}}$  via a series of additive noise into an approximately Gaussian distribution ( $p_{\text{data}} \rightarrow p_t \rightarrow \mathcal{N}(0, I)$  as  $t \rightarrow \infty$ ), described by the stochastic differential equation (SDE) [30]  $d\mathbf{x} = -\frac{\beta_t}{2}\mathbf{x}dt + \sqrt{\beta_t}d\mathbf{w}$ , where  $\mathbf{w}$  is a standard Wiener process, and the drift and diffusion coefficients are parameterized by a monotonically increasing noise scheduler  $\beta_t \in (0, 1)$  in time  $t$  [27]. Reversing the forward diffusion process is described by [110]

$$d\mathbf{x} = [-\frac{\beta_t}{2}\mathbf{x} - \beta_t \nabla_{\mathbf{x}_t} \log p_t(\mathbf{x}_t)] dt + \sqrt{\beta_t}d\mathbf{w} \quad (2)$$

with  $dt$  moving backward in time. In discrete steps that would be from  $T$  to 0. This reverse SDE can be used to generate (sample) data from the distribution  $p_{\text{data}}$ , where the unknown gradient  $\nabla_{\mathbf{x}_t} \log p_t(\mathbf{x}_t)$  can be approximated by a scoring function  $s_\theta(\mathbf{x}_t, t)$ , parameterized by a neural network, and learned via denoising score matching methods [111, 31]. Solving inverse problems is described as a conditional generation where the data is sampled from the posterior  $p(\mathbf{x}|\mathbf{y})$ , i.e.,

$$d\mathbf{x} = [-\frac{\beta_t}{2}\mathbf{x}dt - \beta_t(\nabla_{\mathbf{x}_t} \log p_t(\mathbf{x}_t) + \nabla_{\mathbf{x}_t} \log p_t(\mathbf{y}|\mathbf{x}_t))]dt + \sqrt{\beta_t}d\mathbf{w} \quad (3)$$

For solving general inverse problems where the diffusion is *pre-trained* unconditionally, the prior score  $\nabla_{\mathbf{x}_t} \log p_t(\mathbf{x}_t)$  can be estimated using  $s_\theta(\mathbf{x}_t, t)$ . However, the likelihood score  $\nabla_{\mathbf{x}_t} \log p_t(\mathbf{y}|\mathbf{x}_t)$  is only known at  $t = 0$ , otherwise it is computationally intractable.

**Challenges of training-free diffusion models for inverse problems.** Given the intractability of the likelihood,  $p_t(\mathbf{y}|\mathbf{x}_t) = \int p(\mathbf{y}|\mathbf{x}_0)p_t(\mathbf{x}_0|\mathbf{x}_t)d\mathbf{x}_0$ , training-free diffusion models account assumptions on  $p_t(\mathbf{x}_0|\mathbf{x}_t)$ . The most popular approximation is the isotropic Gaussian approximation  $\mathcal{N}(\mathbf{x}_{0|t}, r_t^2 \mathbf{I})$  [32, 38, 60, 39, 40]. With an optimal denoising score  $s_\theta(\mathbf{x}_t, t)$ , the posterior expectation  $\mathbf{x}_{0|t} := \mathbb{E}[\mathbf{x}_0|\mathbf{x}_t]$  can be computed via Tweedie’s formula. While this offers an MMSE estimation of the posterior expectation, for complex distributions, there is no guarantee that the distribution  $p_t(\mathbf{x}_0|\mathbf{x}_t)$  is concentrated around its mean. From the manifold perspective, this can be interpreted as having a posterior expectation that does not lie on the data manifold  $\mathcal{M}$ . Error in this estimation can propagate beyond the likelihood score into the whole posterior sampling process. Our proposed EquiReg aims to regularize the process to account for these errors.

**Equivariance.** An equivariant function respects symmetries under group transformations, i.e.,

**Definition 3.1** (Equivariance). *The function  $f : \mathcal{Z} \rightarrow \mathcal{X}$  under the actions in the group  $G$  is equivariant if  $S_g(f(\mathbf{z})) = f(T_g(\mathbf{z}))$  for all  $\mathbf{z} \in \mathcal{Z}$  and  $g \in G$  where  $T_g : \mathcal{Z} \rightarrow \mathcal{Z}$  is the set of transformations under the symmetry group  $G$ , and  $S_g$  is the transformation corresponding to  $T_g$  operating the output space  $S_g : \mathcal{X} \rightarrow \mathcal{X}$ , for  $g \in G$ .*

While prior work leverages equivariance to directly incorporate symmetries into deep neural networks [90–92, 94, 112, 113], recent studies explore approximate equivariant networks to relax strict mathematical symmetries that may not fully hold in real-world data, aiming to improve performance [114]. Wang et al. [114] proposes a definition of approximate equivariance (Definition 3.2) [114], which reduces to strict equivariance when  $\epsilon = 0$  (Definition 3.1). For such functions, we define the equivariance error (Definition 3.3) to quantify the deviation from perfect symmetry.

**Definition 3.2** (Approximate Equivariance). *Let  $T_g : \mathcal{Z} \rightarrow \mathcal{Z}$  define the set of transformations under the symmetry group  $G$ , where  $g \in G$ . The function  $f : \mathcal{Z} \rightarrow \mathcal{X}$  under the group  $G$  is  $\epsilon$ -approximate equivariant if  $\|S_g(f(\mathbf{z})) - f(T_g(\mathbf{z}))\| \leq \epsilon$  for all  $\mathbf{z} \in \mathcal{Z}$  and  $g \in G$  where  $S_g$  is the transformation corresponding to  $T_g$  operating the output space  $S_g : \mathcal{X} \rightarrow \mathcal{X}$ .*

**Definition 3.3** (Equivariance Error). *The equivariance error of the function  $f : \mathcal{Z} \rightarrow \mathcal{X}$  under the group  $G$  is  $\mathcal{L}_{EE}(f) = \sup_{\mathbf{z}, g} \|S_g(f(\mathbf{z})) - f(T_g(\mathbf{z}))\|$  where  $T_g : \mathcal{Z} \rightarrow \mathcal{Z}$  is the set of transformations under the symmetry group  $G$ ,  $S_g$  is the transformation corresponding to  $T_g$  operating on the output space  $S_g : \mathcal{X} \rightarrow \mathcal{X}$  for  $g \in G$ . Hence,  $f$  is  $\epsilon$ -approximate equivariant iff  $\mathcal{L}_{EE}(f) < \epsilon$ .*

**Data manifold hypothesis.** Let data  $\mathbf{x} \in \mathcal{X} \subset \mathbb{R}^d$  be in an ambient space of dimension  $d$  with support  $\mathcal{X}$  distribution. We assume that data are sampled from a low-dimensional manifold  $\mathcal{M}$  [115, 116] embedded in a high-dimensional space (Assumption 3.1). This data hypothesis is popular in machine learning [117], and has been studied mathematically in the literature [118, 116, 119, 120]. Moreover, empirical evidence in image processing supports the manifold hypothesis [121, 122], and prior diffusion-based inverse solvers assume this manifold property [62, 33, 32].

**Assumption 3.1** (Manifold Hypothesis). *Let  $\mathbf{x} \in \mathcal{X} \subset \mathbb{R}^d$  be a data sample. The support  $\mathcal{X}$  of the data distribution lies on a  $k$  dimensional manifold  $\mathcal{M}$  within an ambient space  $\mathbb{R}^d$  where  $k \ll d$ .*

## 4 EquiReg: Equivariance Regularized Diffusion

We first discuss our proposed generalized regularization framework for improving diffusion-based inverse solvers. Then, we introduce a new class of functions with distribution-dependent equivariance errors. Lastly, we propose two objective losses to regularize diffusion models for inverse problems.



**Generalized regularization of diffusion models for inverse problems.** EquiReg addresses the propagation error caused by the posterior approximation  $p_t(\mathbf{x}_0|\mathbf{x}_t)$  using regularization. This regularization can be used as a plug-in on a diverse range of pixel-based and latent diffusion models. We explain EquiReg in the context of Wasserstein Gradient Flows.

**Proposition 4.1.** *Let  $\rho(\mathbf{x}, t)$  be the distribution of  $\mathbf{x}_{T-t}$  driven by the ideal reverse dynamics (eq. (3)). Then, the evolution of  $\rho$  follows the Wasserstein-2 gradient flow associated with minimizing functional  $\Phi(\rho, t)$  defined as  $\beta_{T-t} \int [\rho\phi(\mathbf{x}, t) + \frac{1}{2}\rho \log \rho] d\mathbf{x}$ , where  $\phi(\mathbf{x}, t) = -(\log p_{T-t}(\mathbf{x}|\mathbf{y}) + \frac{1}{4}\|\mathbf{x}\|^2)$ .*

The dynamics of  $\rho$  remain the same if we replace  $\phi(\mathbf{x}, t)$  with  $\phi_C(\mathbf{x}, t) := \phi(\mathbf{x}, t) - C(t)$  for arbitrary temporal function  $C(t)$ . Without loss of generality, we assume  $\phi_C(\mathbf{x}, t) < 0$  for all  $\mathbf{x}$  and  $t$ . In practice, the density function  $p_{T-t}$  is not available and thus  $\phi_C(\mathbf{x}, t)$  is approximated as  $\hat{\phi}$  with  $p_{T-t}(\mathbf{x}_{T-t}|\mathbf{y}) \approx \tilde{C}p_{T-t}(\mathbf{x}_{T-t})p(\mathbf{y}|\mathbb{E}[\mathbf{x}_0|\mathbf{x}_{T-t}])$  where  $\tilde{C}$  only depends on  $\mathbf{y}$ .

Because the conditional expectation  $\mathbb{E}[\mathbf{x}_0|\mathbf{x}_{T-t}]$  is a linear combination of all candidate  $\mathbf{x}_0$ , the approximation remains relatively accurate when  $T - t$  is small (i.e.,  $\mathbf{x}_{T-t}$  stays close to the data manifold under low noise) but may incur high error for larger  $T - t$ , as shown in Figure 3. To mitigate this, we reweight the contributions to the first term of  $\Phi$ , down-weighting unreliable estimates, and amplifying the reliable ones. The resulting reweighted functional is

$$\tilde{\Phi}(\rho, t) = \beta_{T-t} [Z_t^{-1} \int \rho(\mathbf{x}) \hat{\phi}_C(\mathbf{x}, t) e^{\frac{\mathcal{R}(\mathbf{x})}{\hat{\phi}_C(\mathbf{x}, t)}} d\mathbf{x} + \frac{1}{2} \int \rho(\mathbf{x}) \log \rho(\mathbf{x}) d\mathbf{x}], \quad (4)$$

where  $Z_t = \int e^{\frac{\mathcal{R}(\mathbf{x})}{\hat{\phi}_C(\mathbf{x}, t)}} d\mathbf{x}$  is the normalizing factor, and  $\mathcal{R}(\mathbf{x})$  is a positive regularization that is nearly zero near the data manifold and much larger elsewhere. Intuitively, since  $\hat{\phi}_C < 0$ , the weight is nearly one for  $\mathbf{x}$  near the data manifold and much smaller elsewhere.

**Proposition 4.2.** (Informal) *The evolution of  $\rho$ , the probability distribution of  $\mathbf{x}_{T-t}$  driven by the practical and regularized reverse dynamics (eq. (5)), is an approximation of the Wasserstein-2 gradient flow associated with minimizing  $\tilde{\Phi}$ .*

$$d\mathbf{x} = [-\frac{\beta_t}{2}\mathbf{x}dt - \beta_t \nabla_{\mathbf{x}_t} (\log p_t(\mathbf{x}_t) + \log \int p(\mathbf{y}|\mathbf{x}_0) \tilde{p}_t(\mathbf{x}_0|\mathbf{x}_t) d\mathbf{x}_0 - \mathcal{R}(\mathbf{x}_t))] dt + \sqrt{\beta_t} d\bar{\mathbf{w}} \quad (5)$$

In contrast to our work, most prior approaches focus on locally reducing likelihood error and do not adopt a generalized view of correcting the full functional being minimized. Next, we introduce distribution-dependent equivariance error and show how to design a regularizer with low error on or near the manifold and high error off-manifold.

**Distribution-dependent equivariance errors.** While the literature has primarily studied the equivariance properties of functions for general inputs, we propose a new equivariance error for approximately equivariant functions under the support of an input data distribution (see Definition 4.1).

**Definition 4.1** (Distribution-Dependent Equivariance Error). *The equivariance error of the function  $f : \mathcal{Z} \rightarrow \mathcal{X}$  under the group  $G$  and under the distribution  $p$  is  $\mathcal{L}_{EE}(f, p) = \sup_g \mathbb{E}_{\mathbf{z} \sim p} [\|S_g(f(\mathbf{z})) - f(T_g(\mathbf{z}))\|]$  where  $T_g : \mathcal{Z} \rightarrow \mathcal{Z}$  is the set of transformations under the symmetry group  $G$ ,  $S_g$  is the transformation corresponding to  $T_g$  operating the output space  $S_g : \mathcal{X} \rightarrow \mathcal{X}$ , for  $g \in G$ .*

The above definition enables us to define the equivariance error of trained function mappings for both on and off the manifold data. We leverage this definition in the next section to find functions whose equivariance error is low for on-manifold data and high elsewhere. Moreover, we introduce a new constrained distribution-dependent equivariance error, where the input is implicitly regularized to lie on the manifold  $\mathcal{M}$  in addition to minimizing the equivariance error (Definition 4.2). Both equivariance errors are non-local, defined at the distribution level. When used to regularize the reverse conditional diffusion process, they are computed via local evaluations over the sampled data.

**Definition 4.2** (Manifold Constrained Distribution-Dependent Equivariance Error). *Let  $T_g : \mathcal{Z} \rightarrow \mathcal{Z}$  define the set of transformations under the symmetry group  $G$ , where  $g \in G$ . The manifold constrained equivariance*

error of the function  $f : \mathcal{Z} \rightarrow \mathcal{X}$  under the group  $G$  and under the data distribution  $p$  is  $\mathcal{L}_{EE}^{\mathcal{M}}(f, p) = \sup_g \mathbb{E}_{z \sim p} [\|z - h(S_g^{-1}(f(T_g(z))))\|]$  where  $h : \mathcal{X} \rightarrow \mathcal{Z}$ ,  $S_g$  is the transformation corresponding to  $T_g$  operating the output space  $S_g : \mathcal{X} \rightarrow \mathcal{X}$  of function  $f$ , and decoder-encoder composition of  $f$ - $h$  forms a vanishing-error autoencoder under the manifold  $\mathcal{M}$  (see Appendix for the definition of vanishing-error autoencoders and their usage in prior work).

**Proposed regularization.** Given the aforementioned formulated errors, we are now ready to discuss the choice the function  $f$ . We term a class of *manifold-preferential equivariant* (MPE) functions, whose equivariance error is lower for samples on the data manifold than for off-manifold samples. We consider two approaches for identifying such functions.

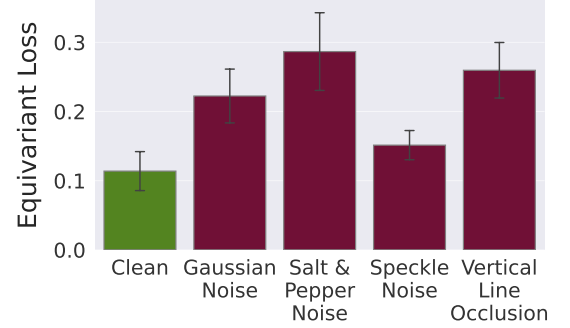
**Training induced equivariance** In this case, MPE emerges via symmetry-preserving augmentations applied during training. Prior work has studied equivariant properties of learned representations in deep networks [123], showing that data augmentations [124] and representation compression by reducing the model capacity [125] promote equivariant features even when equivariance is not explicitly built into the architecture. Importantly, the trained network is only approximately equivariant, and prior studies have sparsely noted that symmetry-preserving properties degrade for inputs deviating from in-distribution data [126]. A few studies have leveraged this emergence of MPE on trained networks for out-of-distribution detection [127–129].

Figure 4a illustrates the MPE property, emergent via training induced equivariance, of  $\mathcal{E}$ - $\mathcal{D}$  of a pre-trained variational autoencoder, currently used in LDMs [61]. Specifically, it shows that the equivariance error is lower for natural images and increases when images deviate from the clean data distribution. Based on Definitions 4.1 and 4.2, we propose *Equi* and *EquiCon* losses using a pre-trained encoder-decoder for diffusion-based inverse solvers such as DPS, PSID, and ReSample.

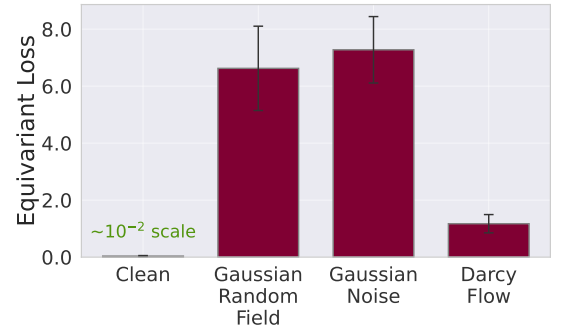
$$\begin{aligned} \text{Equi}_{\text{pixel}} \quad \mathcal{R}(\mathbf{x}_t) &= \|S_g(\mathcal{E}(\mathbf{x}_{0|t})) - \mathcal{E}(T_g(\mathbf{x}_{0|t}))\|_2^2 \\ \text{Equi}_{\text{latent}} \quad \mathcal{R}(\mathbf{z}_t) &= \|S_g(\mathcal{D}(\mathbf{z}_{0|t})) - \mathcal{D}(T_g(\mathbf{z}_{0|t}))\|_2^2 \\ \text{EquiCon}_{\text{latent}} \quad \mathcal{R}(\mathbf{z}_t) &= \|\mathbf{z}_{0|t} - \mathcal{E}(S_g^{-1}(\mathcal{D}(T_g(\mathbf{z}_{0|t}))))\|_2^2 \end{aligned} \quad (6)$$

We use the above regularization for image restoration tasks (e.g., see Algorithm 1 for Equi-DPS).

**Data inherent equivariance** MPE can also emerge naturally from symmetries underlying the data. This often occurs in physics systems where the combination of coefficient functions, boundary values, and solution functions of PDEs remains valid after applying an invertible coordinate transformation consistently to them. Let  $\mathcal{G}(a) \mapsto u$  be a PDE operator that maps from the initial condition  $a$  to the solution  $u$ . Then, it follows that  $S_g(\mathcal{G}(a)) = \mathcal{G}(T_g(a))$ .



(a) Training induced equivariance.



(b) Data inherent equivariance.

Figure 4: **MPE function examples.**

---

#### Algorithm 1 Equi-DPS for Image Restoration Tasks

---

**Require:**  $T, \mathbf{y}, \{\zeta_t\}_{t=1}^T, \{\tilde{\sigma}_t\}_{t=1}^T, \mathbf{s}_\theta, \mathcal{E}, T_g$  and  $S_g, \{\lambda_t\}_{t=1}^T$

- 1:  $\mathbf{x}_T \sim \mathcal{N}(\mathbf{0}, \mathbf{I})$
- 2: **for**  $t = T - 1$  **to** 0 **do**
- 3:    $\hat{\mathbf{s}} \leftarrow \mathbf{s}_\theta(\mathbf{x}_t, t)$
- 4:    $\mathbf{x}_{0|t} \leftarrow \frac{1}{\sqrt{\alpha_t}}(\mathbf{x}_t + (1 - \bar{\alpha}_t)\hat{\mathbf{s}})$
- 5:    $\epsilon \sim \mathcal{N}(\mathbf{0}, \mathbf{I})$
- 6:    $\mathbf{x}'_{t-1} \leftarrow \frac{\sqrt{\alpha_t}(1 - \bar{\alpha}_{t-1})}{1 - \bar{\alpha}_t}\mathbf{x}_t + \frac{\sqrt{\bar{\alpha}_{t-1}\beta_t}}{1 - \bar{\alpha}_t}\mathbf{x}_{0|t} + \tilde{\sigma}_t\epsilon$
- 7:    $\mathbf{x}_{t-1} \leftarrow \mathbf{x}'_{t-1} - \zeta_t \nabla_{\mathbf{x}_t} \|\mathbf{y} - \mathcal{A}(\mathbf{x}_{0|t})\|_2^2$
- 8:    $\mathbf{x}_{t-1} \leftarrow \mathbf{x}_{t-1} - \lambda_t \nabla_{\mathbf{x}_t} \|S_g(\mathcal{E}(\mathbf{x}_{0|t})) - \mathcal{E}(T_g(\mathbf{x}_{0|t}))\|_2^2$
- 9: **end for**
- 10: **return**  $\mathbf{x}_0$

---

We show that models trained on PDEs with inherent symmetries can indeed learn the equivariance property. Neural operators [130] are a popular architecture for modeling physics systems, as their function space setup can preserve the continuum of physics functions and generalize well to different resolutions. Among these, the Fourier Neural Operator (FNO [131]) has drawn the most attention. We train an FNO on the inverse problem of Navier-Stokes, which respects reflection symmetry (see details in Appendix), without explicit data augmentation. As shown in Figure 4b, FNOs trained on non-augmented physics data yield lower equivariance error (Equi<sub>pixel</sub> loss:  $\mathcal{R}(x_t) = \|S_g(\text{FNO}(x_{0|t})) - \text{FNO}(T_g(x_{0|t}))\|_2^2$ ) on in-distribution as opposed to out-of-distribution data.

## 5 Results

This section provides experimental results on the performance of EquiReg for inverse problems, including linear and nonlinear image restoration tasks and reconstructing PDEs. To explore the impact of scaling the noise scheduler, the Appendix includes an experiment on DreamSampler [82], showing preliminary evidence that EquiReg can improve performance on text-to-image guidance.

**Experimental setup for image restorations.** We evaluate the performance of EquiReg when applied to the following three diffusion-based inverse solvers: PSLD [38], ReSample [37], and DPS [32]. Of these methods, PSLD and ReSample are latent solvers, while DPS is a pixel-based solver. We compare against several other methods including DDRM [34], MCG [33], DiffPIR [39], MPGD-AE [62], and DiffStateGrad [41]. We measure performance via perceptual similarity (LPIPS), distribution alignment (FID), pixel-wise fidelity (PSNR), and structural consistency (SSIM). We test EquiReg on two datasets: a) the FFHQ  $256 \times 256$  validation dataset [132], and b) the ImageNet  $256 \times 256$  validation dataset [133]. For pixel-based experiments, we use i) the pre-trained diffusion model from [32] on the FFHQ dataset, and ii) the pre-trained model from [68] on the ImageNet dataset. For latent diffusion experiments, we use i) the unconditional LDM-VQ-4 model [61] on FFHQ, and ii) the Stable Diffusion v1.5 [61] model on ImageNet.

We evaluate EquiReg on a variety of linear and nonlinear restoration tasks for natural images. We fix sets of 100 images from FFHQ and ImageNet as our validation sets. All images are normalized from  $[0, 1]$ . For the majority of experiments, we use noise level  $\sigma_y = 0.05$  (we indicate  $\sigma_y$  in our tables). For linear inverse problems, we consider (1) box inpainting, (2) random inpainting, (3) Gaussian deblur, (4) motion deblur, and (5) super-resolution. We apply a random  $128 \times 128$  pixel box for box inpainting, and a 70% random mask for random inpainting. For Gaussian and motion deblur, we use kernels of size  $61 \times 61$ , with standard deviations of 3.0 and 0.5, respectively. For super-resolution, we downscale images by a factor of 4 using a bicubic resizer. For nonlinear inverse problems, we consider (1) phase retrieval, (2) nonlinear deblur, and (3) high dynamic range (HDR).

Table 1: **Effect of EquiReg on ReSample [37].** Inverse problems on FFHQ  $256 \times 256$  with  $\sigma_y = 0.01$ .

Task	Method	LPIPS↓	FID↓	PSNR↑	SSIM↑
<i>Linear</i>					
Gaussian deblur	ReSample	0.253	55.65	27.78	0.757
	Equi-ReSample	0.197	64.86	<b>29.08</b>	<b>0.825</b>
	EquiCon-ReSample	<b>0.156</b>	<b>54.72</b>	28.18	0.777
Motion deblur	ReSample	0.160	40.14	30.55	0.854
	Equi-ReSample	0.120	46.28	<b>30.92</b>	<b>0.870</b>
	EquiCon-ReSample	<b>0.078</b>	<b>37.61</b>	30.73	0.860
Super-res. ( $\times 4$ )	ReSample	0.204	40.46	28.02	0.790
	Equi-ReSample	<b>0.098</b>	43.56	<b>29.74</b>	<b>0.849</b>
	EquiCon-ReSample	0.112	<b>40.38</b>	28.27	0.801
Box inpainting	ReSample	0.198	108.30	19.91	0.807
	Equi-ReSample	<b>0.150</b>	<b>59.69</b>	<b>22.56</b>	<b>0.832</b>
	EquiCon-ReSample	0.171	110.70	21.04	0.815
Random inpainting	ReSample	0.115	36.12	31.27	0.892
	Equi-ReSample	<b>0.047</b>	29.88	<b>31.47</b>	<b>0.908</b>
	EquiCon-ReSample	<b>0.047</b>	<b>28.81</b>	31.21	0.904
<i>Nonlinear</i>					
HDR	ReSample	0.190	<b>49.06</b>	<b>24.88</b>	<b>0.819</b>
	Equi-ReSample	<b>0.133</b>	49.52	24.71	0.815
	EquiCon-ReSample	0.135	49.98	24.67	0.817
Phase retrieval	ReSample	0.237	97.86	27.61	0.750
	Equi-ReSample	<b>0.155</b>	<b>85.22</b>	<b>28.16</b>	0.770
	EquiCon-ReSample	0.159	88.75	28.11	<b>0.774</b>
Nonlinear deblur	ReSample	0.188	56.06	29.54	0.842
	Equi-ReSample	0.128	55.09	29.45	0.840
	EquiCon-ReSample	<b>0.125</b>	<b>54.62</b>	<b>29.55</b>	<b>0.843</b>

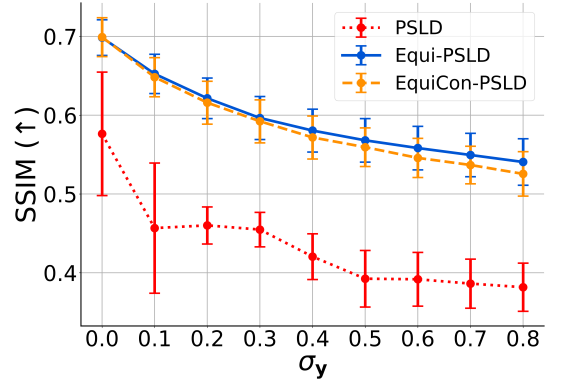


Figure 5: **EquiReg consistently improves performance across a range of measurement noise levels.** Gaussian deblur using FFHQ  $256 \times 256$  for  $\sigma_y = [0, 0.8]$ .



Table 2: Linear inverse problems on FFHQ  $256 \times 256$  with  $\sigma_y = 0.05$ .

Method	Gaussian deblur				Motion deblur				Super-resolution ( $\times 4$ )			
	LPIPS↓	FID↓	PSNR↑	SSIM↑	LPIPS↓	FID↓	PSNR↑	SSIM↑	LPIPS↓	FID↓	PSNR↑	SSIM↑
<i>Latent</i>												
PSLD	0.357	106.2	22.87	0.537	<b>0.322</b>	<b>84.62</b>	24.25	0.615	0.313	89.72	24.51	0.650
Equi-PSLD (ours)	<u>0.344</u>	<u>94.09</u>	<b>24.42</b>	<u>0.657</u>	<u>0.338</u>	99.14	<u>24.83</u>	<u>0.669</u>	<u>0.289</u>	90.88	<b>26.32</b>	<u>0.718</u>
EquiCon-PSLD (ours)	<b>0.320</b>	<b>83.18</b>	<u>24.38</u>	<b>0.664</b>	<b>0.322</b>	<u>89.87</u>	<b>25.14</b>	<b>0.699</b>	<b>0.277</b>	<b>79.39</b>	<u>26.14</u>	<b>0.722</b>
<i>Pixel-based</i>												
DDRM	0.239	92.43	24.93	0.732	-	-	-	-	0.282	79.25	26.58	<b>0.782</b>
MCG	0.340	101.2	6.72	0.051	0.702	310.5	6.72	0.055	0.520	87.64	20.05	0.559
DiffPIR	0.236	59.65	<b>27.36</b>	-	0.255	65.78	26.57	-	0.260	<u>65.77</u>	<u>26.64</u>	-
MPGD-AE	0.150	114.9	24.42	0.664	0.120	104.5	25.72	0.723	<u>0.168</u>	137.7	24.01	0.670
DPS	0.145	104.8	25.48	0.709	0.132	99.75	26.75	0.754	0.191	125.4	24.38	0.675
DiffStateGrad-DPS	<u>0.128</u>	<u>52.73</u>	26.29	<u>0.739</u>	<u>0.118</u>	<u>50.14</u>	<u>27.61</u>	<u>0.782</u>	0.186	73.02	24.65	0.683
Equi-DPS (ours)	<b>0.114</b>	<b>48.76</b>	<u>26.32</u>	<b>0.750</b>	<b>0.094</b>	<b>41.71</b>	<b>28.23</b>	<b>0.810</b>	<b>0.120</b>	<b>51.00</b>	<b>27.15</b>	<u>0.776</u>

(a) Deblurring and super-resolution linear inverse problems.

Method	Box inpainting				Random inpainting			
	LPIPS↓	FID↓	PSNR↑	SSIM↑	LPIPS↓	FID↓	PSNR↑	SSIM↑
<i>Latent</i>								
PSLD	0.158	43.02	<u>24.22</u>	0.819	0.246	49.77	29.05	0.809
Equi-PSLD (ours)	<u>0.098</u>	<b>31.54</b>	24.19	<u>0.875</u>	<b>0.188</b>	<u>41.61</u>	<b>30.43</b>	<b>0.878</b>
EquiCon-PSLD (ours)	<b>0.092</b>	<u>35.07</u>	<b>24.26</b>	<b>0.884</b>	<u>0.204</u>	<b>40.75</b>	<u>29.99</u>	<u>0.847</u>
<i>Pixel-based</i>								
DDRM	0.207	78.62	22.26	0.801	0.218	-	25.75	-
MCG	0.309	<b>40.11</b>	19.97	0.703	0.286	<b>29.26</b>	21.57	0.751
MPGD-AE	0.138	248.7	21.59	0.753	0.172	339.0	25.22	0.732
DPS	0.133	56.89	23.10	0.799	0.113	51.32	29.63	0.849
DiffStateGrad-DPS	<u>0.114</u>	47.53	<b>24.10</b>	<u>0.831</u>	<u>0.107</u>	49.42	<u>30.15</u>	<u>0.852</u>
Equi-DPS (ours)	<b>0.099</b>	<u>40.47</u>	<u>23.39</u>	<b>0.835</b>	<b>0.068</b>	<u>33.65</u>	<b>32.16</b>	<b>0.902</b>

(b) Inpainting linear inverse problems.

 Table 3: Linear inverse problems on ImageNet  $256 \times 256$  with  $\sigma_y = 0.05$ .

Method	Gaussian deblur		Motion deblur		Super-resolution ( $\times 4$ )		Box inpainting		Random inpainting	
	FID↓	PSNR↑	FID↓	PSNR↑	FID↓	PSNR↑	FID↓	PSNR↑	FID↓	PSNR↑
PSLD	263.9	20.70	252.1	21.26	224.3	22.29	151.4	16.28	83.22	26.56
EquiCon-PSLD (ours)	<b>214.5</b>	<b>22.01</b>	<b>196.3</b>	<b>22.69</b>	<b>198.5</b>	<b>22.34</b>	<b>137.6</b>	<b>19.25</b>	<b>65.14</b>	<b>27.03</b>

We use an oversampling rate of 2.0 for phase retrieval, and due to instability of the task, we generate four independent reconstructions and take the best result (as also done in DPS [32], DAPS [40], and DiffStateGrad [41]). We use the default setting from [134] for nonlinear deblur, and a scale factor of 2 for HDR.

For these tasks, we adopt the pre-trained encoder-decoder  $\mathcal{E}-\mathcal{D}$  as our MPE function. For FFHQ, the symmetry group contains reflection (across vertical axis). For ImageNet, we define a rotation group  $G = \{\pi/2, 3\pi/2\}$ , and uniformly at random select the group action for each sample. Finally, the loss functions given in Equation (6) are used as regularization terms.

**Image restoration performance.** Our results (Tables 1 to 3) show that EquiReg improves the performance of several methods across a wide variety of linear and nonlinear tasks on both FFHQ and ImageNet. EquiReg significantly improves performance on box inpainting when applied to ReSample (Table 1). We attribute this improvement in part to the reduction of failure cases (Figure 6).

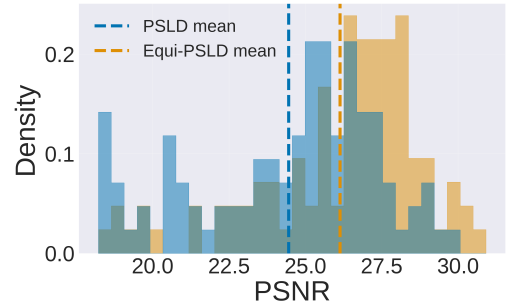


Figure 6: EquiReg reduces failure cases and enhances reconstruction fidelity. Super-resolution using FFHQ  $256 \times 256$ .

We observe that EquiReg achieves its largest improvements on perceptual metrics (FID and LPIPS), suggesting that it generates more realistic images that lie closer to the data manifold (see Appendix for supporting qualitative results). Moreover, EquiReg improves performance under high measurement noise (Figure 5). This result aligns with Figure 4a, which shows the equivariance error is lower on clean images than noisy ones, indicating that EquiReg enforces an effective denoising.

**PDE reconstruction tasks.** We evaluate the performance of EquiReg on two important PDE problems: the Helmholtz and Navier-Stokes equations (see Appendix). The objective is to solve both forward and inverse problems in sparse sensor settings. The forward problem involves predicting the solution function or the final state using measurements from only 3% of the coefficient field or the initial state. The inverse problem, conversely, aims to predict the input conditions from observations of 3% of the system’s output. This task is challenging due to the nonlinearity of the equations, the complex structure of Gaussian random fields, and the sparsity of observations.

Recent studies [51, 56, 57] have demonstrated the superiority of diffusion-based approaches over deterministic single-forward methods for PDE reconstructions. DiffusionPDE [51] decomposes the conditional log-likelihood into a data prior (from a pre-trained diffusion model) and a measurement score, thereby providing solutions via conditional sampling. FunDPS [56, 57] further extends the sampling process to a more natural infinite-dimensional spaces, achieving better accuracy and speed via function space models.

We integrate EquiReg into the state-of-the-art FunDPS framework [56, 57], computing the Equi loss using data inherent equivariance derived from an FNO trained on the corresponding inverse problem. For our experiments, we use reflection symmetry (i.e., flipping along the  $y = x$  axis), and observe no significant performance difference when using other transformations such as rotations or alternating flips. As shown in Table 4, Equi-FunDPS improves performance, measured by relative  $\ell_2$  loss—across various tasks, especially in inverse problems where a strong data prior is critical.

Table 4: **Partially-observed PDE reconstruction.**

	Steps ( $N$ )	Helmholtz		Navier-Stokes	
		Forward	Inverse	Forward	Inverse
DiffusionPDE	2000	12.64%	19.07%	3.78%	9.63%
FunDPS	500	2.13%	17.16%	3.32%	8.48%
Equi-FunDPS (ours)	500	<b>2.12%</b>	<b>15.91%</b>	<b>3.06%</b>	<b>7.84%</b>

## 6 Conclusion

We introduce *Equivariance Regularized* (EquiReg) diffusion for solving inverse problems. EquiReg corrects errors introduced in posterior approximations by regularizing the sampling trajectories so they lie closer to the data manifold. Our method applies to many inverse problem settings across diverse domains and is flexible to the choice of diffusion model and sampling method.

**Limitations and future work.** EquiReg’s effectiveness relies on the quality of the pre-trained diffusion prior. In addition, we do not address the approximations of the underlying diffusion models, but we regularize them for improved performance. Moreover, applying EquiReg requires task-specific regularizer design: one must choose an appropriate symmetry group and identify suitable MPE functions for each problem setting. As a result of this task-specific design, EquiReg can be explored in many other problem settings where equivariance is training induced or data inherent. We leave this for future work.

## 7 Acknowledgements and Contributions

Aditi worked on this project as part of her bachelor’s thesis. Anima was supported by Bren Chair Professor and AI2050 Senior Fellow.

Bahareh proposed and led the project. Aditi and Rayhan implemented the method and executed all the image restoration experiments. Abbas conducted the text-to-image experiments, and Jiachen performed the PDE reconstruction experiments. Bahareh wrote the original draft of the paper with Aditi, Rayhan, and Jiachen writing the results section. The project was originally based on training-induced MPE functions, proposed by Bahareh. Later versions of the project include data-inherent MPE functions, proposed by Jiachen; this is used for the PDE experiments. Bahareh, Abbas, Jiachen, and Chuwei collaborated on formalizing the theory, and the final formulation of Wasserstein gradient flow was proposed and proven by Chuwei. All authors provided editorial comments and feedback on the manuscript. Anima supervised the project and provided valuable feedback.



## References

- [1] Charles W Groetsch and CW Groetsch. *Inverse problems in the mathematical sciences*, volume 52. Springer, 1993.
- [2] Harrison H Barrett and Kyle J Myers. *Foundations of image science*. John Wiley & Sons, 2013.
- [3] Idris A Elbakri and Jeffrey A Fessler. Statistical image reconstruction for polyenergetic x-ray computed tomography. *IEEE transactions on medical imaging*, 21(2):89–99, 2002.
- [4] Michael Lustig, David Donoho, and John M Pauly. Sparse mri: The application of compressed sensing for rapid mr imaging. *Magnetic Resonance in Medicine: An Official Journal of the International Society for Magnetic Resonance in Medicine*, 58(6):1182–1195, 2007.
- [5] Michael Elad. *Sparse and redundant representations: from theory to applications in signal and image processing*. Springer Science & Business Media, 2010.
- [6] Michael Elad, Mario AT Figueiredo, and Yi Ma. On the role of sparse and redundant representations in image processing. *Proceedings of the IEEE*, 98(6):972–982, 2010.
- [7] Jianchao Yang, John Wright, Thomas S Huang, and Yi Ma. Image Super-resolution via Sparse Representation. *IEEE transactions on image processing*, 19(11):2861–2873, 2010.
- [8] Mario Bertero, Patrizia Boccacci, and Christine De Mol. *Introduction to inverse problems in imaging*. CRC press, 2021.
- [9] MN Oğuztöreli and TM Caelli. An inverse problem in neural processing. *Biological cybernetics*, 53(4):239–245, 1986.
- [10] Kenji Nose-Filho, Andre Kazuo Takahata, Renato Lopes, and Joao Marcos Travassos Romano. Improving Sparse Multichannel Blind Deconvolution with Correlated Seismic Data: Foundations and Further Results. *IEEE Signal Processing Magazine*, 35(2):41–50, 2018.
- [11] Richard Baraniuk and Philippe Steeghs. Compressive radar imaging. In *2007 IEEE radar conference*, pages 128–133. IEEE, 2007.
- [12] Lee C Potter, Emre Ertin, Jason T Parker, and Müjdat Cetin. Sparsity and compressed sensing in radar imaging. *Proceedings of the IEEE*, 98(6):1006–1020, 2010.
- [13] Mark D Plumbley, Thomas Blumensath, Laurent Daudet, Rémi Gribonval, and Mike E Davies. Sparse representations in audio and music: from coding to source separation. *Proceedings of the IEEE*, 98(6):995–1005, 2009.
- [14] Nasser Kazemi and Mauricio D Sacchi. Sparse multichannel blind deconvolution. *Geophysics*, 79(5):V143–V152, 2014.
- [15] Bahareh Tolooshams, Sourav Dey, and Demba Ba. Deep residual autoencoders for expectation maximization-inspired dictionary learning. *IEEE Transactions on neural networks and learning systems*, 32(6):2415–2429, 2020.
- [16] Kazunori Akiyama, Kazuki Kuramochi, Shiro Ikeda, Vincent L Fish, Fumie Tazaki, Mareki Honma, Sheperd S Doleman, Avery E Broderick, Jason Dexter, Monika Mościbrodzka, et al. Imaging the Schwarzschild-radius-scale Structure of M87 with the Event Horizon Telescope using Sparse Modeling. *The Astrophysical Journal*, 838(1):1, 2017.
- [17] Sergei Igorevich Kabanikhin. Definitions and examples of inverse and ill-posed problems. 2008.

- [18] Andrew M Stuart. Inverse problems: a bayesian perspective. *Acta numerica*, 19:451–559, 2010.
- [19] David L Donoho. Compressed sensing. *IEEE Transactions on information theory*, 52(4):1289–1306, 2006.
- [20] Emmanuel J Candès, Justin Romberg, and Terence Tao. Robust uncertainty principles: Exact signal reconstruction from highly incomplete frequency information. *IEEE Transactions on information theory*, 52(2):489–509, 2006.
- [21] Emmanuel J Candès and Michael B Wakin. An introduction to compressive sampling. *IEEE signal processing magazine*, 25(2):21–30, 2008.
- [22] Miles Lopes. Estimating unknown sparsity in compressed sensing. In *International Conference on Machine Learning*, pages 217–225. PMLR, 2013.
- [23] Trevor Hastie, Robert Tibshirani, and Martin Wainwright. *Statistical learning with sparsity: the lasso and generalizations*. CRC press, 2015.
- [24] Andrew Waters, Aswin Sankaranarayanan, and Richard Baraniuk. Sparcs: Recovering low-rank and sparse matrices from compressive measurements. *Advances in neural information processing systems*, 24, 2011.
- [25] Emmanuel J Candès, Xiaodong Li, Yi Ma, and John Wright. Robust principal component analysis? *Journal of the ACM (JACM)*, 58(3):1–37, 2011.
- [26] Gene H Golub, Per Christian Hansen, and Dianne P O’Leary. Tikhonov regularization and total least squares. *SIAM journal on matrix analysis and applications*, 21(1):185–194, 1999.
- [27] Jonathan Ho, Ajay Jain, and Pieter Abbeel. Denoising diffusion probabilistic models. *Advances in neural information processing systems*, 33:6840–6851, 2020.
- [28] Yang Song and Stefano Ermon. Generative Modeling by Estimating Gradients of the Data Distribution. In *Advances in Neural Information Processing Systems*, volume 32, 2019.
- [29] Yang Song and Stefano Ermon. Improved Techniques for Training Score-Based Generative Models. In *Advances in Neural Information Processing Systems*, volume 33, pages 12438–12448, 2020.
- [30] Yang Song, Jascha Sohl-Dickstein, Diederik Kingma, Abhishek Kumar, Stefano Ermon, and Ben Poole. Score-based Generative Modeling through Stochastic Differential Equations. In *The International Conference on Learning Representations*, 2021. URL <https://openreview.net/pdf/ef0eadbe07115b0853e964f17aa09d811cd490f1.pdf>.
- [31] Pascal Vincent. A Connection Between Score Matching and Denoising Autoencoders. *Neural Computation*, 23(7):1661–1674, 2011. doi: 10.1162/NECO\_a\_00142.
- [32] Hyungjin Chung, Jeongsol Kim, Michael Thompson Mccann, Marc Louis Klasky, and Jong Chul Ye. Diffusion Posterior Sampling for General Noisy Inverse Problems. In *The Eleventh International Conference on Learning Representations*, 2023. URL <https://openreview.net/forum?id=0nD9zGAGT0k>.
- [33] Hyungjin Chung, Byeongsu Sim, Dohoon Ryu, and Jong Chul Ye. Improving Diffusion Models for Inverse Problems using Manifold Constraints. *Advances in Neural Information Processing Systems*, 35:25683–25696, 2022.
- [34] Bahjat Kwar, Michael Elad, Stefano Ermon, and Jiaming Song. Denoising diffusion restoration models. *Advances in Neural Information Processing Systems*, 35:23593–23606, 2022.
- [35] Andreas Lugmayr, Martin Danelljan, Andres Romero, Fisher Yu, Radu Timofte, and Luc Van Gool. Repaint: Inpainting using denoising diffusion probabilistic models. In *Proceedings of the IEEE/CVF conference on computer vision and pattern recognition*, pages 11461–11471, 2022.

- [36] Chitwan Saharia, Jonathan Ho, William Chan, Tim Salimans, David J Fleet, and Mohammad Norouzi. Image super-resolution via iterative refinement. *IEEE transactions on pattern analysis and machine intelligence*, 45(4):4713–4726, 2022.
- [37] Bowen Song, Soo Min Kwon, Zecheng Zhang, Xinyu Hu, Qing Qu, and Liyue Shen. Solving Inverse Problems with Latent Diffusion Models via Hard Data Consistency. In *Conference on Parsimony and Learning (Recent Spotlight Track)*, 2023. URL <https://openreview.net/forum?id=iHcarDCZLn>.
- [38] Litu Rout, Negin Raoof, Giannis Daras, Constantine Caramanis, Alex Dimakis, and Sanjay Shakkottai. Solving Linear Inverse Problems Provably via Posterior Sampling with Latent Diffusion Models. In *Thirty-seventh Conference on Neural Information Processing Systems*, 2023. URL <https://openreview.net/forum?id=XKBFdYwfRo>.
- [39] Yuanzhi Zhu, Kai Zhang, Jingyun Liang, Jiezhong Cao, Bihan Wen, Radu Timofte, and Luc Van Gool. Denoising diffusion models for plug-and-play image restoration. In *Proceedings of the IEEE/CVF Conference on Computer Vision and Pattern Recognition*, pages 1219–1229, 2023.
- [40] Bingliang Zhang, Wenda Chu, Julius Berner, Chenlin Meng, Anima Anandkumar, and Yang Song. Improving Diffusion Inverse Problem Solving with Decoupled Noise Annealing. *arXiv preprint arXiv:2407.01521*, 2024.
- [41] Rayhan Zirvi, Bahareh Tolooshams, and Anima Anandkumar. Diffusion state-guided projected gradient for inverse problems. In *The Thirteenth International Conference on Learning Representations*, 2025. URL <https://openreview.net/forum?id=kRBQwlkFSP>.
- [42] Yang Song, Liyue Shen, Lei Xing, and Stefano Ermon. Solving Inverse Problems in Medical Imaging with Score-Based Generative Models. In *International Conference on Learning Representations*, 2022.
- [43] Hyungjin Chung and Jong Chul Ye. Score-Based Diffusion Models for Accelerated MRI. *Medical Image Analysis*, page 102479, 2022.
- [44] Hyungjin Chung, Eun Sun Lee, and Jong Chul Ye. MR Image Denoising and Super-Resolution Using Regularized Reverse Diffusion. *IEEE Transactions on Medical Imaging*, 42(4):922–934, 2022.
- [45] Alex Ling Yu Hung, Kai Zhao, Haoxin Zheng, Ran Yan, Steven S Raman, Demetri Terzopoulos, and Kyunghyun Sung. Med-CDiff: Conditional Medical Image Generation with Diffusion Models. *Bioengineering*, 10(11):1258, 2023.
- [46] Zolnamar Dorjsembe, Hsing-Kuo Pao, Sodtivilan Odonchimed, and Furen Xiao. Conditional Diffusion Models for Semantic 3D Brain MRI Synthesis. *IEEE Journal of Biomedical and Health Informatics*, 2024.
- [47] Guangyuan Li, Chen Rao, Juncheng Mo, Zhanjie Zhang, Wei Xing, and Lei Zhao. Rethinking diffusion model for multi-contrast mri super-resolution. In *Proceedings of the IEEE/CVF Conference on Computer Vision and Pattern Recognition*, pages 11365–11374, 2024.
- [48] Amirhossein Kazerouni, Ehsan Khodapanah Aghdam, Moein Heidari, Reza Azad, Mohsen Fayyaz, Ilker Hacihaliloglu, and Dorit Merhof. Diffusion models in medical imaging: A comprehensive survey. *Medical image analysis*, 88:102846, 2023.
- [49] Wanyu Bian, Albert Jang, Liping Zhang, Xiaonan Yang, Zachary Stewart, and Fang Liu. Diffusion modeling with domain-conditioned prior guidance for accelerated mri and qmri reconstruction. *IEEE Transactions on Medical Imaging*, 2024.
- [50] Victor Isakov. *Inverse problems for Partial Differential Equations*, volume 127. Springer, 2006.



- [51] Jiahe Huang, Guandao Yang, Zichen Wang, and Jeong Joon Park. DiffusionPDE: Generative PDE-solving under partial observation. In *The Thirty-eighth Annual Conference on Neural Information Processing Systems*, 2024.
- [52] Aliaksandra Shysheya, Cristiana Diaconu, Federico Bergamin, Paris Perdikaris, José Miguel Hernández-Lobato, Richard Turner, and Emile Mathieu. On conditional diffusion models for pde simulations. *Advances in Neural Information Processing Systems*, 37:23246–23300, 2024.
- [53] Ziming Liu, Di Luo, Yilun Xu, Tommi Jaakkola, and Max Tegmark. Genphys: From physical processes to generative models. *arXiv preprint arXiv:2304.02637*, 2023.
- [54] Zijie Li, Anthony Zhou, and Amir Barati Farimani. Generative latent neural pde solver using flow matching. *arXiv preprint arXiv:2503.22600*, 2025.
- [55] Lorenzo Baldassari, Ali Siahkoobi, Josselin Garnier, Knut Solna, and Maarten V de Hoop. Conditional score-based diffusion models for bayesian inference in infinite dimensions. *Advances in Neural Information Processing Systems*, 36:24262–24290, 2023.
- [56] Abbas Mammadov, Julius Berner, Kamyar Azizzadenesheli, Jong Chul Ye, and Anima Anandkumar. Diffusion-based inverse solver on function spaces with applications to pdes. *Machine Learning and the Physical Sciences Workshop at NeurIPS*, 2024. URL [https://ml4physicalsciences.github.io/2024/files/NeurIPS\\_ML4PS\\_2024\\_253.pdf](https://ml4physicalsciences.github.io/2024/files/NeurIPS_ML4PS_2024_253.pdf).
- [57] Jiachen Yao, Abbas Mammadov, Julius Berner, Gavin Kerrigan, Jong Chul Ye, Kamyar Azizzadenesheli, and Anima Anandkumar. Guided diffusion sampling on function spaces with applications to pdes, 2025. URL <https://arxiv.org/abs/2505.17004>.
- [58] Abbas Mammadov, Hyungjin Chung, and Jong Chul Ye. Amortized posterior sampling with diffusion prior distillation, 2024. URL <https://arxiv.org/abs/2407.17907>.
- [59] Gabriel Cardoso, Yazid Janati el idrissi, Sylvain Le Corff, and Eric Moulines. Monte carlo guided denoising diffusion models for bayesian linear inverse problems. In *The Twelfth International Conference on Learning Representations*, 2024. URL <https://openreview.net/forum?id=nHESwXvxWK>.
- [60] Jiaming Song, Arash Vahdat, Morteza Mardani, and Jan Kautz. Pseudoinverse-Guided Diffusion Models for Inverse Problems. 2023. URL [https://openreview.net/forum?id=9\\_gsMA8MRKQ](https://openreview.net/forum?id=9_gsMA8MRKQ).
- [61] Robin Rombach, Andreas Blattmann, Dominik Lorenz, Patrick Esser, and Björn Ommer. High-resolution Image Synthesis with Latent Diffusion Models. In *Proceedings of the IEEE/CVF conference on computer vision and pattern recognition*, pages 10684–10695, 2022.
- [62] Yutong He, Naoki Murata, Chieh-Hsin Lai, Yuhta Takida, Toshimitsu Uesaka, Dongjun Kim, Wei-Hsiang Liao, Yuki Mitsufuji, J Zico Kolter, Ruslan Salakhutdinov, and Stefano Ermon. Manifold preserving guided diffusion. In *International Conference on Learning Representations*, 2024.
- [63] Xinyu Peng, Ziyang Zheng, Wenrui Dai, Nuoqian Xiao, Chenglin Li, Junni Zou, and Hongkai Xiong. Improving diffusion models for inverse problems using optimal posterior covariance. In *Forty-first International Conference on Machine Learning*, 2024.
- [64] Litu Rout, Yujia Chen, Abhishek Kumar, Constantine Caramanis, Sanjay Shakkottai, and Wen-Sheng Chu. Beyond first-order tweedie: Solving inverse problems using latent diffusion. In *Proceedings of the IEEE/CVF Conference on Computer Vision and Pattern Recognition*, pages 9472–9481, 2024.
- [65] Benjamin Boys, Mark Girolami, Jakiw Pidstrigach, Sebastian Reich, Alan Mosca, and Omer Deniz Akyildiz. Tweedie moment projected diffusions for inverse problems. *Transactions on Machine Learning Research*, 2024. ISSN 2835-8856. URL <https://openreview.net/forum?id=4unJi0qrTE>. Featured Certification.

- [66] Jascha Sohl-Dickstein, Eric Weiss, Niru Maheswaranathan, and Surya Ganguli. Deep unsupervised learning using nonequilibrium thermodynamics. In *International conference on machine learning*, pages 2256–2265. pmlr, 2015.
- [67] Zahra Kadkhodaie and Eero Simoncelli. Stochastic solutions for linear inverse problems using the prior implicit in a denoiser. *Advances in Neural Information Processing Systems*, 34:13242–13254, 2021.
- [68] Prafulla Dhariwal and Alexander Nichol. Diffusion models beat gans on image synthesis. *Advances in neural information processing systems*, 34:8780–8794, 2021.
- [69] Patrick Esser, Sumith Kulal, Andreas Blattmann, Rahim Entezari, Jonas Müller, Harry Saini, Yam Levi, Dominik Lorenz, Axel Sauer, Frederic Boesel, et al. Scaling rectified flow transformers for high-resolution image synthesis. In *Forty-first international conference on machine learning*, 2024.
- [70] Giannis Daras, Weili Nie, Karsten Kreis, Alex Dimakis, Morteza Mardani, Nikola Kovachki, and Arash Vahdat. Warped diffusion: Solving video inverse problems with image diffusion models. *Advances in Neural Information Processing Systems*, 37:101116–101143, 2024.
- [71] Andreas Blattmann, Tim Dockhorn, Sumith Kulal, Daniel Mendelevitch, Maciej Kilian, Dominik Lorenz, Yam Levi, Zion English, Vikram Voleti, Adam Letts, et al. Stable video diffusion: Scaling latent video diffusion models to large datasets. *arXiv preprint arXiv:2311.15127*, 2023.
- [72] Tim Brooks, Bill Peebles, Connor Holmes, Will DePue, Yufei Guo, Li Jing, David Schnurr, Joe Taylor, Troy Luhman, Eric Luhman, et al. Video generation models as world simulators. *OpenAI Blog*, 1:8, 2024.
- [73] Bingliang Zhang, Zihui Wu, Berthy T Feng, Yang Song, Yisong Yue, and Katherine L Bouman. Step: A general and scalable framework for solving video inverse problems with spatiotemporal diffusion priors. *preprint arXiv:2504.07549*, 2025.
- [74] Lvmin Zhang, Anyi Rao, and Maneesh Agrawala. Adding conditional control to text-to-image diffusion models. In *Proceedings of the IEEE/CVF international conference on computer vision*, pages 3836–3847, 2023.
- [75] Nupur Kumari, Bingliang Zhang, Sheng-Yu Wang, Eli Shechtman, Richard Zhang, and Jun-Yan Zhu. Ablating concepts in text-to-image diffusion models. In *Proceedings of the IEEE/CVF International Conference on Computer Vision*, pages 22691–22702, 2023.
- [76] Nataniel Ruiz, Yuanzhen Li, Varun Jampani, Yael Pritch, Michael Rubinstein, and Kfir Aberman. Dream-booth: Fine tuning text-to-image diffusion models for subject-driven generation. In *Proceedings of the IEEE/CVF conference on computer vision and pattern recognition*, pages 22500–22510, 2023.
- [77] Shihao Zhao, Dongdong Chen, Yen-Chun Chen, Jianmin Bao, Shaozhe Hao, Lu Yuan, and Kwan-Yee K Wong. Uni-controlnet: All-in-one control to text-to-image diffusion models. *Advances in Neural Information Processing Systems*, 36:11127–11150, 2023.
- [78] Gunshi Gupta, Karmesh Yadav, Yarin Gal, Dhruv Batra, Zsolt Kira, Cong Lu, and Tim GJ Rudner. Pre-trained text-to-image diffusion models are versatile representation learners for control. *Advances in Neural Information Processing Systems*, 37:74182–74210, 2024.
- [79] Berthy T Feng, Jamie Smith, Michael Rubinstein, Huiwen Chang, Katherine L Bouman, and William T Freeman. Score-based diffusion models as principled priors for inverse imaging. In *Proceedings of the IEEE/CVF International Conference on Computer Vision*, pages 10520–10531, 2023.
- [80] Berthy Feng and Katherine Bouman. Variational bayesian imaging with an efficient surrogate score-based prior. *Transactions on Machine Learning Research*, 2024. ISSN 2835-8856. URL <https://openreview.net/forum?id=db2pFKVcm1>.

- [81] Morteza Mardani, Jiaming Song, Jan Kautz, and Arash Vahdat. A variational perspective on solving inverse problems with diffusion models. In *The Twelfth International Conference on Learning Representations*, 2024.
- [82] Jeongsol Kim, Geon Yeong Park, and Jong Chul Ye. Dreamsampler: Unifying diffusion sampling and score distillation for image manipulation. In *European Conference on Computer Vision*, pages 398–414. Springer, 2024.
- [83] Jonathan Ho and Tim Salimans. Classifier-free diffusion guidance. *arXiv preprint arXiv:2207.12598*, 2022.
- [84] Arash Vahdat, Karsten Kreis, and Jan Kautz. Score-based generative modeling in latent space. *Advances in neural information processing systems*, 34:11287–11302, 2021.
- [85] William Peebles and Saining Xie. Scalable diffusion models with transformers. In *Proceedings of the IEEE/CVF international conference on computer vision*, pages 4195–4205, 2023.
- [86] Yinhuai Wang, Jiwen Yu, and Jian Zhang. Zero-shot image restoration using denoising diffusion null-space model. In *The Eleventh International Conference on Learning Representations*, 2023.
- [87] Herbert Ellis Robbins. An empirical bayes approach to statistics. In *Proc. Third Berkley Symposium on Mathematical Statistics*, pages 157–163, 1956.
- [88] Koichi Miyasawa et al. An empirical bayes estimator of the mean of a normal population. *Bull. Inst. Internat. Statist.*, 38(181-188):1–2, 1961.
- [89] Bradley Efron. Tweedie’s formula and selection bias. *Journal of the American Statistical Association*, 106(496):1602–1614, 2011.
- [90] Michael M Bronstein, Joan Bruna, Taco Cohen, and Petar Veličković. Geometric deep learning: Grids, groups, graphs, geodesics, and gauges. *preprint arXiv:2104.13478*, 2021.
- [91] Victor Garcia Satorras, Emiel Hoogeboom, and Max Welling. E (n) equivariant graph neural networks. In *International conference on machine learning*, pages 9323–9332. PMLR, 2021.
- [92] Taco Cohen and Max Welling. Group equivariant convolutional networks. In *International conference on machine learning*, pages 2990–2999. PMLR, 2016.
- [93] David W Romero and Suhas Lohit. Learning partial equivariances from data. *Advances in Neural Information Processing Systems*, 35:36466–36478, 2022.
- [94] Marc Finzi, Samuel Stanton, Pavel Izmailov, and Andrew Gordon Wilson. Generalizing convolutional neural networks for equivariance to lie groups on arbitrary continuous data. In *International Conference on Machine Learning*, pages 3165–3176. PMLR, 2020.
- [95] Benjamin Bloem-Reddy, Yee Whye, et al. Probabilistic symmetries and invariant neural networks. *Journal of Machine Learning Research*, 21(90):1–61, 2020.
- [96] Dian Wang, Stephen Hart, David Surovik, Tarik Kelestemur, Haojie Huang, Haibo Zhao, Mark Yeatman, Jiuguang Wang, Robin Walters, and Robert Platt. Equivariant diffusion policy. In *8th Annual Conference on Robot Learning*, 2024. URL <https://openreview.net/forum?id=wD2kUULT1g>.
- [97] Emiel Hoogeboom, Victor Garcia Satorras, Clément Vignac, and Max Welling. Equivariant diffusion for molecule generation in 3d. In *International conference on machine learning*, pages 8867–8887, 2022.
- [98] Jiaqi Guan, Wesley Wei Qian, Xingang Peng, Yufeng Su, Jian Peng, and Jianzhu Ma. 3d equivariant diffusion for target-aware molecule generation and affinity prediction. In *The Eleventh International Conference on Learning Representations*, 2023.

- [99] Jiaqi Guan, Xingang Peng, Peiqi Jiang, Yunan Luo, Jian Peng, and Jianzhu Ma. Linkernet: Fragment poses and linker co-design with 3d equivariant diffusion. *Advances in Neural Information Processing Systems*, 36:77503–77519, 2023.
- [100] François Cornet, Grigory Bartosh, Mikkel Schmidt, and Christian Andersson Naesseth. Equivariant neural diffusion for molecule generation. *Advances in Neural Information Processing Systems*, 37:49429–49460, 2024.
- [101] Kehua Chen, Xianda Chen, Zihan Yu, Meixin Zhu, and Hai Yang. Equidiff: A conditional equivariant diffusion model for trajectory prediction. In *2023 IEEE 26th International Conference on Intelligent Transportation Systems (ITSC)*, pages 746–751. IEEE, 2023.
- [102] Johann Brehmer, Joey Bose, Pim De Haan, and Taco S Cohen. Edgi: Equivariant diffusion for planning with embodied agents. *Advances in Neural Information Processing Systems*, 36:63818–63834, 2023.
- [103] Rui Jiao, Wenbing Huang, Peijia Lin, Jiaqi Han, Pin Chen, Yutong Lu, and Yang Liu. Crystal structure prediction by joint equivariant diffusion. *Advances in Neural Information Processing Systems*, 36:17464–17497, 2023.
- [104] Eloi Moliner, Jaakko Lehtinen, and Vesa Välimäki. Solving audio inverse problems with a diffusion model. In *ICASSP 2023 - 2023 IEEE International Conference on Acoustics, Speech and Signal Processing (ICASSP)*, pages 1–5, 2023.
- [105] Jérémy Scanvic, Mike Davies, Patrice Abry, and Julián Tachella. Scale-equivariant imaging: Self-supervised learning for image super-resolution and deblurring. 2025.
- [106] Dongdong Chen, Mike Davies, Matthias J Ehrhardt, Carola-Bibiane Schönlieb, Ferdia Sherry, and Julián Tachella. Imaging with equivariant deep learning: From unrolled network design to fully unsupervised learning. *IEEE Signal Processing Magazine*, 40(1):134–147, 2023.
- [107] Matthieu Terris, Thomas Moreau, Nelly Pustelnik, and Julian Tachella. Equivariant plug-and-play image reconstruction. In *Proceedings of the IEEE/CVF Conference on Computer Vision and Pattern Recognition*, pages 25255–25264, 2024.
- [108] Julián Tachella, Dongdong Chen, and Mike Davies. Sensing theorems for unsupervised learning in linear inverse problems. *Journal of Machine Learning Research*, 24(39):1–45, 2023.
- [109] Hannah Lawrence, Vasco Portilheiro, Yan Zhang, and Sékou-Oumar Kaba. Improving equivariant networks with probabilistic symmetry breaking. *International Conference on Learning Representations*, 2025.
- [110] Brian DO Anderson. Reverse-time diffusion equation models. *Stochastic Processes and their Applications*, 12(3):313–326, 1982.
- [111] Aapo Hyvärinen and Peter Dayan. Estimation of non-normalized statistical models by score matching. *Journal of Machine Learning Research*, 6(4), 2005.
- [112] Nathaniel Thomas, Tess Smidt, Steven Kearnes, Lusann Yang, Li Li, Kai Kohlhoff, and Patrick Riley. Tensor field networks: Rotation-and translation-equivariant neural networks for 3d point clouds. *arXiv preprint arXiv:1802.08219*, 2018.
- [113] Fabian Fuchs, Daniel Worrall, Volker Fischer, and Max Welling. Se (3)-transformers: 3d roto-translation equivariant attention networks. *Advances in neural information processing systems*, 33:1970–1981, 2020.
- [114] Rui Wang, Robin Walters, and Rose Yu. Approximately equivariant networks for imperfectly symmetric dynamics. In *International Conference on Machine Learning*, pages 23078–23091. PMLR, 2022.

- [115] Lawrence Cayton et al. *Algorithms for manifold learning*. eScholarship, University of California, 2008.
- [116] Yunqian Ma and Yun Fu. *Manifold learning theory and applications*, volume 434. CRC press Boca Raton, 2012.
- [117] Sebastian Bordt, Uddeshya Upadhyay, Zeynep Akata, and Ulrike von Luxburg. The manifold hypothesis for gradient-based explanations. In *Proceedings of the IEEE/CVF Conference on Computer Vision and Pattern Recognition*, pages 3697–3702, 2023.
- [118] Hariharan Narayanan and Sanjoy Mitter. Sample complexity of testing the manifold hypothesis. *Advances in neural information processing systems*, 23, 2010.
- [119] Nick Whiteley, Annie Gray, and Patrick Rubin-Delanchy. Statistical exploration of the manifold hypothesis. *arXiv preprint arXiv:2208.11665*, 2022.
- [120] Valentin De Bortoli. Convergence of denoising diffusion models under the manifold hypothesis. *Transactions on Machine Learning Research*, 2022. ISSN 2835-8856. URL <https://openreview.net/forum?id=MhK5aXo3gB>.
- [121] Kilian Q Weinberger and Lawrence K Saul. Unsupervised learning of image manifolds by semidefinite programming. *International journal of computer vision*, 70:77–90, 2006.
- [122] Charles Fefferman, Sanjoy Mitter, and Hariharan Narayanan. Testing the manifold hypothesis. *Journal of the American Mathematical Society*, 29(4):983–1049, 2016.
- [123] Karel Lenc and Andrea Vedaldi. Understanding image representations by measuring their equivariance and equivalence. In *Proceedings of the IEEE conference on computer vision and pattern recognition*, pages 991–999, 2015.
- [124] Alex Krizhevsky, Ilya Sutskever, and Geoffrey E Hinton. Imagenet classification with deep convolutional neural networks. *Advances in neural information processing systems*, 25, 2012.
- [125] Robert-Jan Bruintjes, Tomasz Motyka, and Jan van Gemert. What affects learned equivariance in deep image recognition models? In *Proceedings of the IEEE/CVF Conference on Computer Vision and Pattern Recognition*, pages 4839–4847, 2023.
- [126] Aharon Azulay and Yair Weiss. Why do deep convolutional networks generalize so poorly to small image transformations? *Journal of Machine Learning Research*, 20(184):1–25, 2019.
- [127] Yibo Zhou. Rethinking reconstruction autoencoder-based out-of-distribution detection. In *Proceedings of the IEEE/CVF Conference on Computer Vision and Pattern Recognition*, pages 7379–7387, 2022.
- [128] Ramneet Kaur, Susmit Jha, Anirban Roy, Sangdon Park, Edgar Dobriban, Oleg Sokolsky, and Insup Lee. idecode: In-distribution equivariance for conformal out-of-distribution detection. In *Proceedings of the AAAI conference on artificial intelligence*, volume 36, pages 7104–7114, 2022.
- [129] Ramneet Kaur, Kaustubh Sridhar, Sangdon Park, Yahan Yang, Susmit Jha, Anirban Roy, Oleg Sokolsky, and Insup Lee. Codit: Conformal out-of-distribution detection in time-series data for cyber-physical systems. In *Proceedings of the ACM/IEEE 14th International Conference on Cyber-Physical Systems (with CPS-IoT Week 2023)*, pages 120–131, 2023.
- [130] Nikola B. Kovachki, Zongyi Li, Burigede Liu, Kamyar Azizzadenesheli, Kaushik Bhattacharya, Andrew M. Stuart, and Anima Anandkumar. Neural operator: Learning maps between function spaces. *CoRR*, abs/2108.08481, 2021.

- [131] Zongyi Li, Nikola Borislavov Kovachki, Kamyar Azizzadenesheli, Kaushik Bhattacharya, Andrew Stuart, Anima Anandkumar, et al. Fourier neural operator for parametric partial differential equations. In *International Conference on Learning Representations*, 2021.
- [132] Tero Karras, Samuli Laine, and Timo Aila. A Style-Based Generator Architecture for Generative Adversarial Networks. *IEEE Transactions on Pattern Analysis & Machine Intelligence*, 43(12):4217–4228, Dec 2021.
- [133] Jia Deng, Wei Dong, Richard Socher, Li-Jia Li, Kai Li, and Li Fei-Fei. ImageNet: A Large-Scale Hierarchical Image Database. In *2009 IEEE Conference on Computer Vision and Pattern Recognition*, pages 248–255. IEEE, 2009.
- [134] Phong Tran, Anh Tran, Quynh Phung, and Minh Hoai. Explore Image Deblurring via Encoded Blur Kernel Space. In *Proceedings of the IEEE/CVF Conference on Computer Vision and Pattern Recognition (CVPR)*. IEEE, 2021.
- [135] Zongyi Li, Nikola Kovachki, Kamyar Azizzadenesheli, Burigede Liu, Kaushik Bhattacharya, Andrew Stuart, and Anima Anandkumar. Fourier neural operator for parametric partial differential equations. *arXiv preprint arXiv:2010.08895*, 2020.
- [136] Richard Jordan, David Kinderlehrer, and Felix Otto. The variational formulation of the fokker–planck equation. *SIAM journal on mathematical analysis*, 29(1):1–17, 1998.
- [137] Christopher A Metzler, Arian Maleki, and Richard G Baraniuk. From denoising to compressed sensing. *IEEE Transactions on Information Theory*, 62(9):5117–5144, 2016.
- [138] Yaniv Romano, Michael Elad, and Peyman Milanfar. The little engine that could: Regularization by denoising (red). *SIAM Journal on Imaging Sciences*, 10(4):1804–1844, 2017.
- [139] Kai Zhang, Wangmeng Zuo, Shuhang Gu, and Lei Zhang. Learning deep cnn denoiser prior for image restoration. In *Proceedings of the IEEE conference on computer vision and pattern recognition*, pages 3929–3938, 2017.
- [140] Chris Metzler, Ali Mousavi, and Richard Baraniuk. Learned d-amp: Principled neural network based compressive image recovery. *Advances in neural information processing systems*, 30, 2017.
- [141] Diederik P Kingma. Auto-encoding Variational Bayes. *arXiv preprint arXiv:1312.6114*, 2013.
- [142] Ian Goodfellow, Jean Pouget-Abadie, Mehdi Mirza, Bing Xu, David Warde-Farley, Sherjil Ozair, Aaron Courville, and Yoshua Bengio. Generative Adversarial Nets. *Advances in neural information processing systems*, 27, 2014.
- [143] Ashish Bora, Ajil Jalal, Eric Price, and Alexandros G Dimakis. Compressed Sensing using Generative Models. In *International conference on machine learning*, pages 537–546. PMLR, 2017.
- [144] Ajil Jalal, Marius Arvinte, Giannis Daras, Eric Price, Alexandros G Dimakis, and Jon Tamir. Robust Compressed Sensing MRI with Deep Generative Priors. In *Advances in Neural Information Processing Systems*, volume 34, pages 14938–14954. Curran Associates, Inc., 2021.
- [145] Hang Shao, Abhishek Kumar, and P Thomas Fletcher. The riemannian geometry of deep generative models. In *Proceedings of the IEEE Conference on Computer Vision and Pattern Recognition Workshops*, pages 315–323, 2018.
- [146] Christopher Anders, Plamen Pasliev, Ann-Kathrin Dombrowski, Klaus-Robert Müller, and Pan Kessel. Fairwashing explanations with off-manifold detergent. In *International Conference on Machine Learning*, pages 314–323. PMLR, 2020.



## Appendices

We provide our source code when EquiReg is implemented on DPS. This supplementary materials contain the following:

- [Appendix A](#) includes additional experiments on text-to-image guidance. We regularize DreamSampler [82] with EquiReg for an improved performance (see [Figures 7 to 10](#)).
- [Appendix B](#) includes additional image restoration experiments for ImageNet. We show that EquiReg improves LatentDAPS and DPS across several different inverse problems ([Table 5](#), [Table 6](#)).
- [Appendix C](#) reports standard deviations on experiments done on PS LD (see [Table 7](#)).
- [Appendix D](#) includes qualitative analysis on the performance of methods with and without EquiReg. Results show a reduction of artifacts and an improved perceptual quality of the solution. This section also includes the equivariance error of a pre-trained encoder used in EquiReg ([Figure 11a](#)), an equivariant loss vs. Gaussian noise plot ([Figure 12](#)), and a histogram of Equi’s improvement on DPS ([Figure 13](#)).
- [Appendix E](#) demonstrates EquiReg implementation for PS LD, ReSample, DPS, and LatentDAPS ([Algorithm 2](#), [Algorithm 3](#), [Algorithm 4](#), [Algorithm 5](#), [Algorithm 6](#), [Algorithm 7](#)). It also contains information about the EquiReg hyperparameters for image restoration tasks.
- [Appendix F](#) contains information on the PDE reconstruction experiment. It discusses the equations along with implementation details and hyperparameters.
- [Appendix G](#) provides theoretical proof of [Propositions 4.1](#) and [4.2](#).
- [Appendix H](#) contains additional background information on solving inverse problems, vanishing-error autoencoders, and equivariance.
- [Appendix I](#) discloses computing resources used to conduct the experiments.
- [Appendix J](#) credits code assets used for our experiments.
- [Appendix K](#) discusses the broader impacts of this paper, the developed method, the conducted experiments, and their overall implications.
- [Appendix L](#) concludes the appendix with a “responsible release” statement.

## A EquiReg for Text-to-Image Guidance

Given the “source” image, DreamSampler [82] is asked to transform the source image using the prompt. Applying EquiReg to DreamSampler, we observe perceptual improvement of generated images as well as artifact reduction. Figure 7 shows a cat, as the source image, being transformed into “corgi”, “croissant”, “cat statue”, and “fluffy dog”. Equi-DreamSampler generates more realistic images than DreamSampler (e.g., EquiReg modifies the three front legged corgi to two front legs).

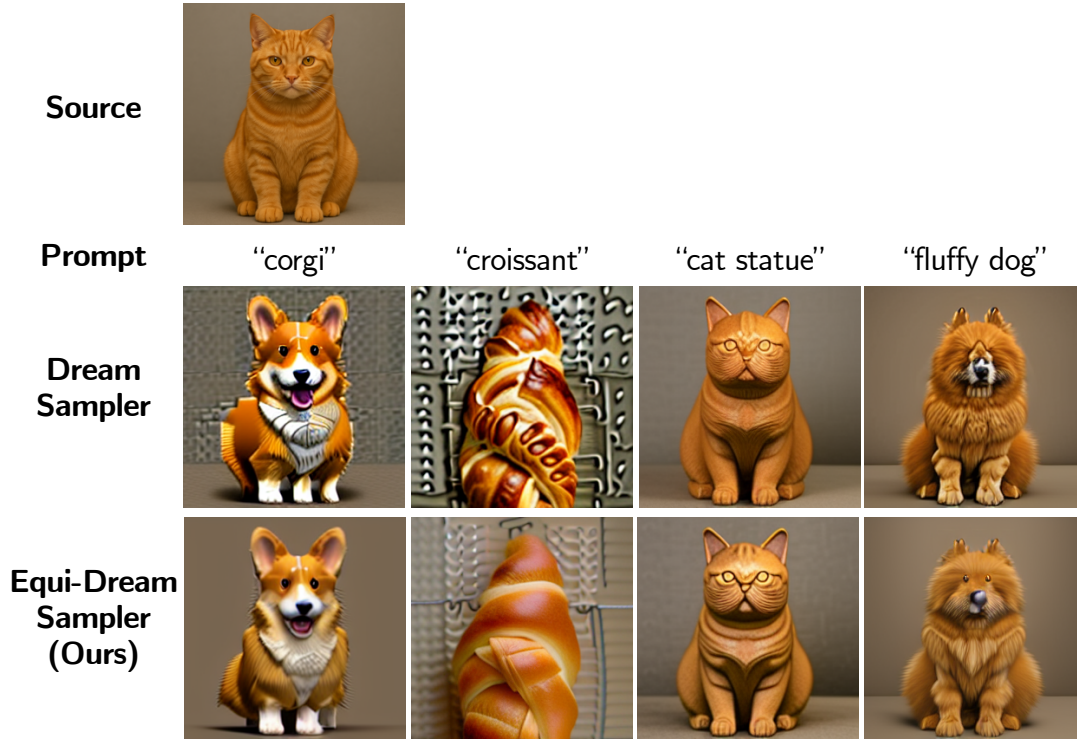


Figure 7: EquiReg helps the text-guided DreamSampler generate more realistic images.

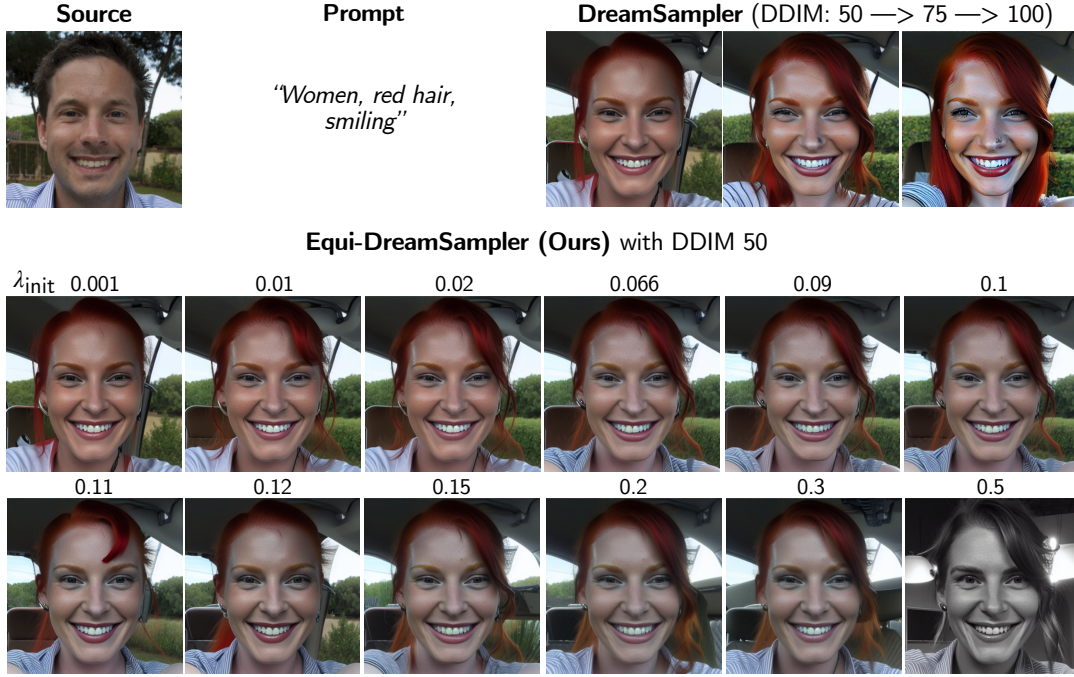


Figure 8: **Impact of EquiReg parameter  $\lambda$ , implicit acceleration, and introduction of more image details.** Women, red hair, smiling.

We have also observed an implicit acceleration of image generation when EquiReg is imposed (Figure 8). Equi-DreamSampler with 50 DDIM steps can generate images that are only possible with DreamSampler when the DDIM steps are increased. We attribute this to EquiReg’s ability to generate images that are closer to the data manifold. For example, the increase of DDIM steps in DreamSampler (from 50 to 75 to 100) has a relatively similar effect to increasing the EquiReg regularizer  $\lambda$  at a fixed 50 DDIM steps. Figure 8 shows that increasing the regularization  $\lambda$  results in addition of a car in the background. For DreamSampler, an early notion of the car seat in the background start to arise only when DDIM is increased to 100 (see also Figures 9 and 10).

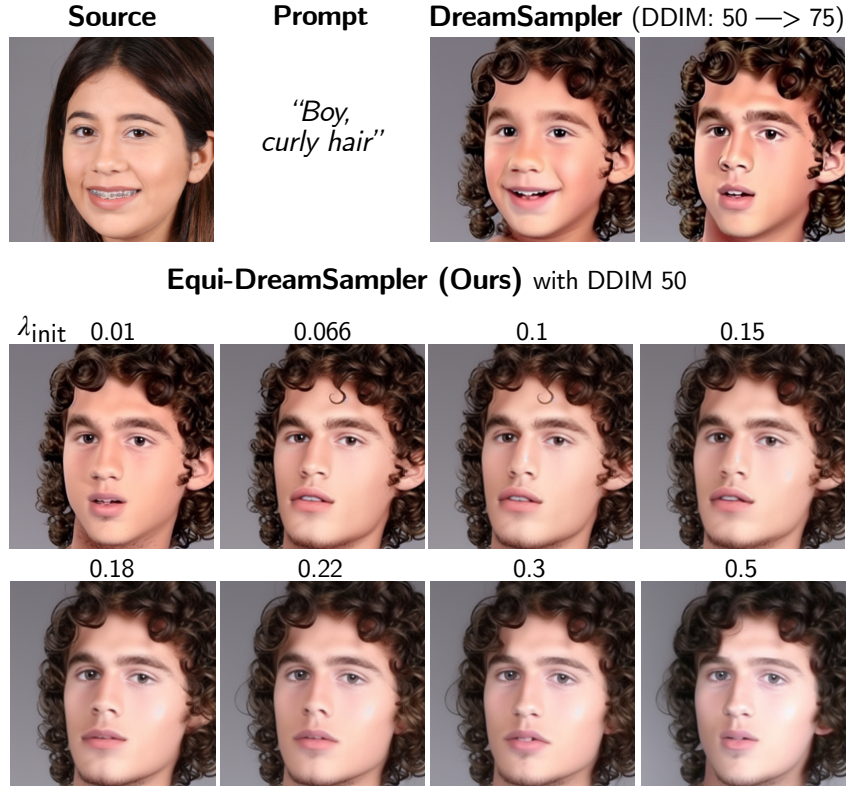


Figure 9: Adding EquiReg into the text-to-image guidance method DreamSampler for improved performance. Boy, curly hair.

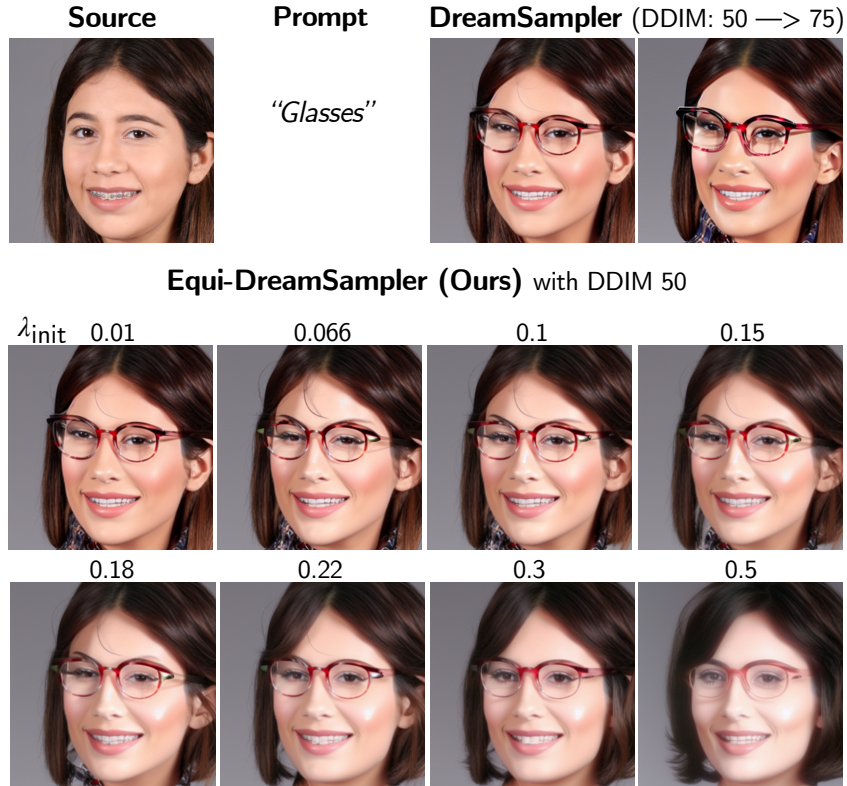


Figure 10: Adding EquiReg into the text-to-image guidance method DreamSampler for improved performance. Glasses.

## B Additional Experiments on Image Restoration Tasks

We show two additional results. EquiReg improves LatentDAPS performance on ImageNet for box inpainting and motion deblur (Table 5). Moreover, Equi-DPS performs much better than DPS, increasing the PSNR from 20.70 to 23.45 dB for super-resolution on ImageNet (Table 6).

Table 5: **Equi-LatentDAPS vs. LatentDAPS on ImageNet  $256 \times 256$  with  $\sigma_y = 0.05$ .**

Method	Box inpainting		Motion deblur	
	LPIPS↓	PSNR↑	LPIPS↓	PSNR↑
LatentDAPS	0.310	20.19	0.305	25.08
Equi-LatentDAPS (ours)	<b>0.299</b>	<b>20.67</b>	<b>0.286</b>	<b>25.86</b>

Table 6: **Equi-DPS vs. DPS on ImageNet  $256 \times 256$  with  $\sigma_y = 0.05$ .**

Method	Super-resolution ( $\times 4$ )		Random inpainting	
	FID↓	PSNR↑	FID↓	PSNR↑
DPS	169.6	20.70	94.83	25.96
Equi-DPS (ours)	<b>102.7</b>	<b>23.45</b>	<b>55.87</b>	<b>28.32</b>

## C Additional Information on Image Restoration Tasks

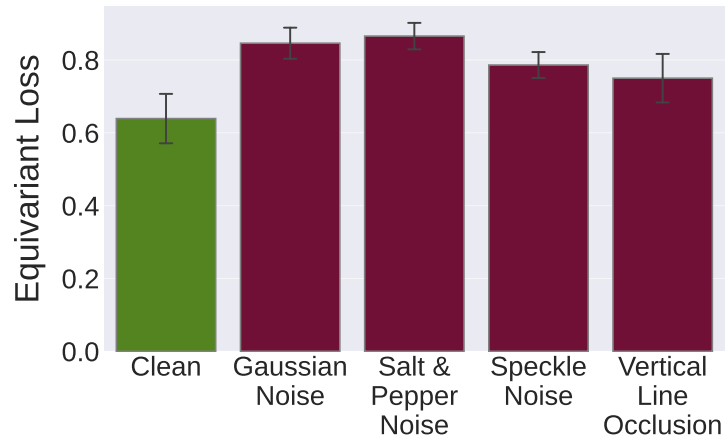
We report standard deviation on all linear tasks for PSLD, Equi-PSLD, and EquiCon-PSLD (Table 7).

Table 7: **Reporting standard deviations.** Inverse problems on FFHQ  $256 \times 256$  with  $\sigma_y = 0.05$ .

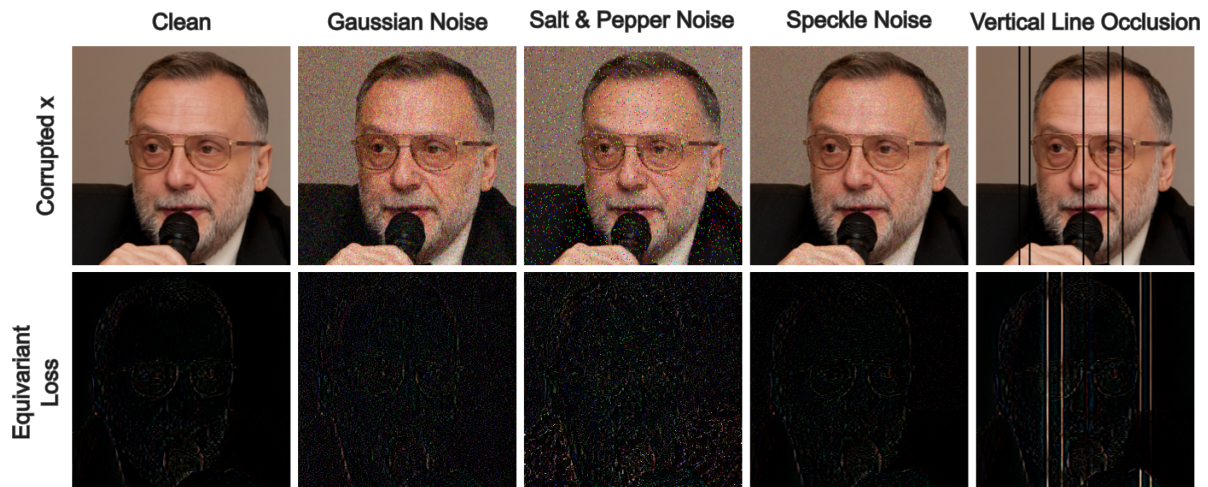
Task	Method	LPIPS↓	PSNR↑	SSIM↑
Gaussian deblur	PSLD	0.357 (0.060)	22.87 (1.67)	0.537 (0.094)
	Equi-PSLD (ours)	0.344 (0.055)	24.42 (1.66)	0.657 (0.076)
	EquiCon-PSLD (ours)	0.320 (0.048)	24.38 (1.55)	0.664 (0.068)
Motion deblur	PSLD	0.322 (0.048)	24.25 (1.47)	0.615 (0.075)
	Equi-PSLD (ours)	0.338 (0.052)	24.83 (1.75)	0.669 (0.068)
	EquiCon-PSLD (ours)	0.322 (0.054)	25.14 (1.62)	0.699 (0.064)
Super-res. ( $\times 4$ )	PSLD	0.313 (0.098)	24.51 (2.98)	0.650 (0.140)
	Equi-PSLD (ours)	0.289 (0.088)	26.32 (2.24)	0.718 (0.104)
	EquiCon-PSLD (ours)	0.277 (0.093)	26.14 (2.74)	0.722 (0.119)
Box inpainting	PSLD	0.158 (0.023)	24.22 (2.80)	0.819 (0.031)
	Equi-PSLD (ours)	0.098 (0.019)	24.19 (2.67)	0.875 (0.027)
	EquiCon-PSLD (ours)	0.092 (0.021)	24.26 (2.80)	0.884 (0.029)
Random inpainting	PSLD	0.246 (0.053)	29.05 (1.98)	0.809 (0.049)
	Equi-PSLD (ours)	0.188 (0.034)	30.43 (1.76)	0.878 (0.027)
	EquiCon-PSLD (ours)	0.204 (0.051)	29.99 (2.06)	0.847 (0.047)



## D Visualizations for Image Restoration Experiments



(a) The equivariance error of the encoder is lower on clean, natural images than corrupted ones.



(b) Example visualizations of used images.

Figure 11: **Training induced equivariance for a pre-trained encoder.** Experimental setup corresponds to [Figure 4a](#) in the main text, which uses a pre-trained decoder.

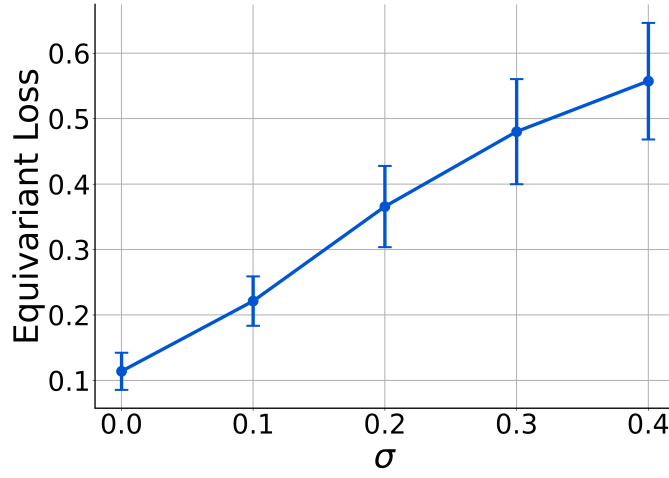


Figure 12: **Equivariance error of a pre-trained decoder over different Gaussian noise levels  $\sigma$ .** We apply different Gaussian noise levels to clean images to see the effect of noise on equivariance error. We observe that as Gaussian noise increases, equivariance error increases steadily.

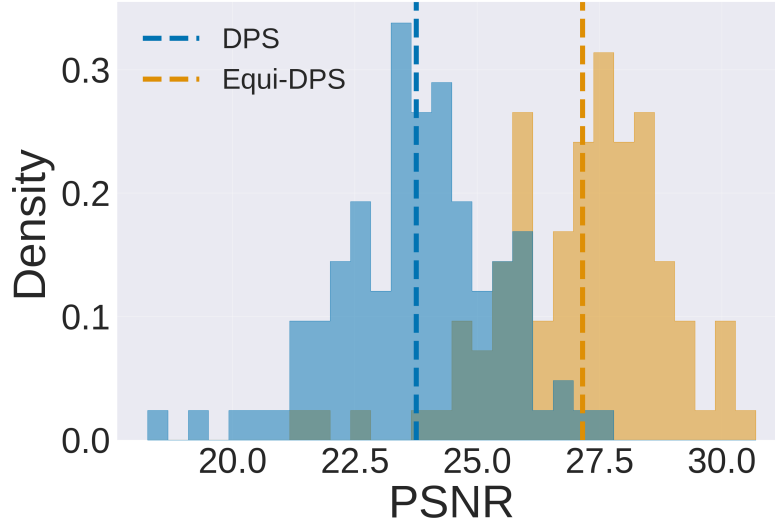
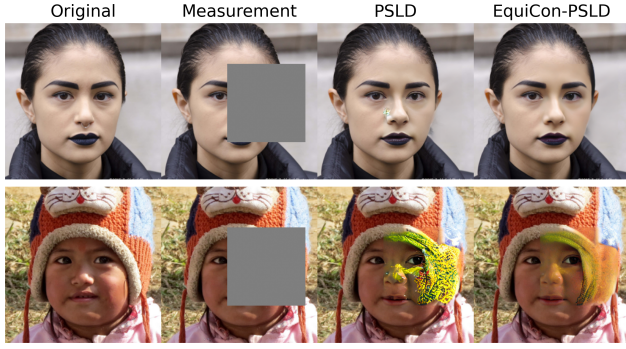
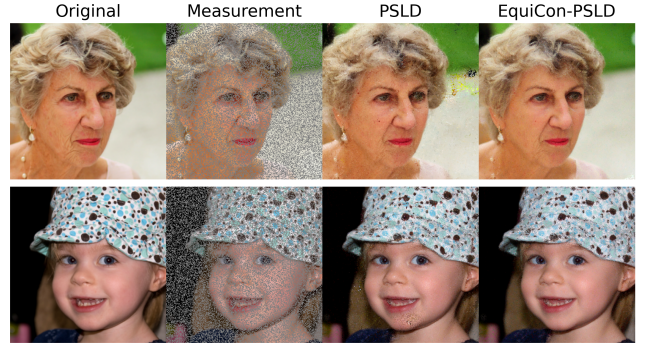


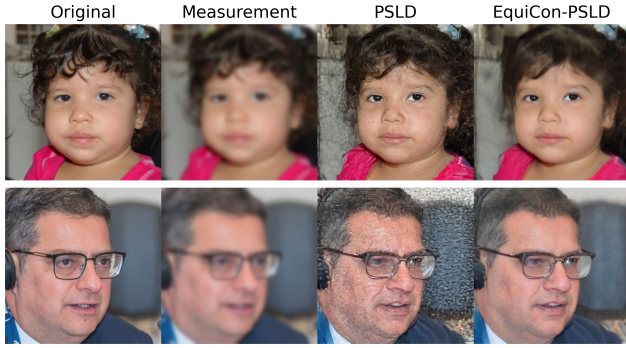
Figure 13: **Histogram of EquiReg improvement for DPS.** Super-resolution using FFHQ  $256 \times 256$ .



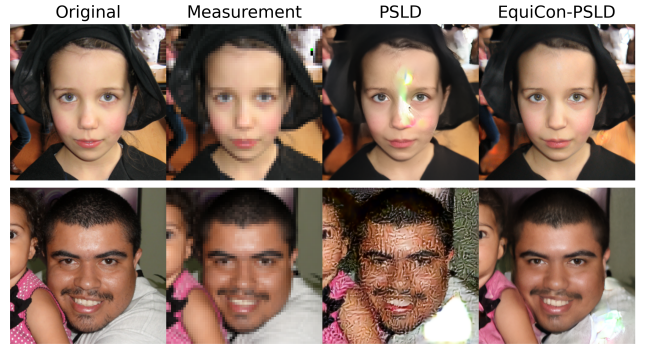
(a) Box inpainting.



(b) Random inpainting.

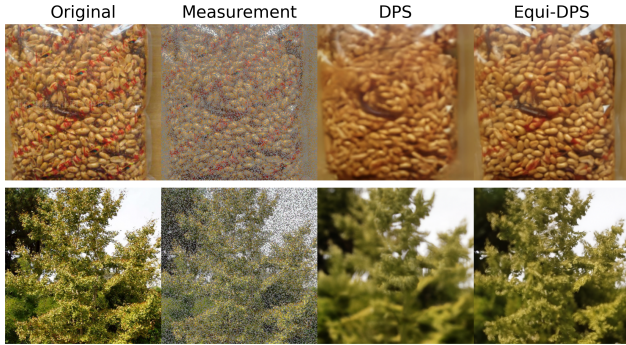


(c) Gaussian deblur.

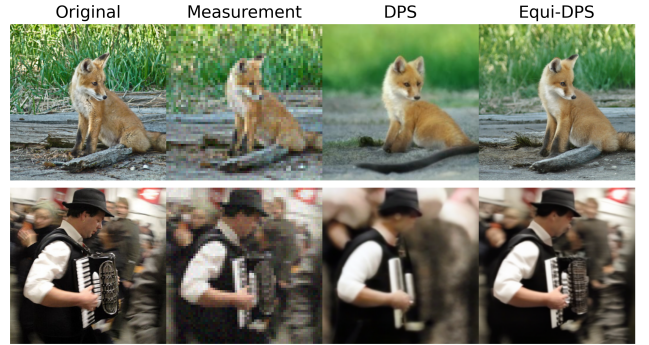


(d) Super-resolution ( $\times 4$ ).

Figure 14: Qualitative comparison of EquiCon-PSLD and PSLD on FFHQ  $256 \times 256$ .



(a) Random inpainting.



(b) Super-resolution ( $\times 4$ ).

Figure 15: Qualitative comparison of Equi-DPS and DPS on ImageNet  $256 \times 256$ .

## E Implementation Details for Image Restoration Tasks

**Hyperparameters.** Our method introduces a single hyperparameter  $\lambda$  that controls the amount of regularization applied. Below we include a table detailing the use of this hyperparameter in the main experiments (Table 8). For majority of experiments, we keep  $\lambda$  constant throughout iterations. However, we note that in our Equi-DPS and Equi-LatentDAPS experiments, we scale  $\lambda$  by the noise scheduler at every iteration. For all unscaled experiments, we employ early stopping, setting  $\lambda = 0$  for the last 10% of sampling.

Table 8: Equivariance regularization weight  $\lambda$  used in main experiments.

Method	Box Inpainting	Random Inpainting	Gaussian Deblur	Motion Deblur	Super-resolution ( $\times 4$ )
<i>FFHQ</i> $256 \times 256$					
Equi-PSLD	0.05	0.05	0.03	0.03	0.02
EquiCon-PSLD	0.01	0.01	0.01	0.01	0.01
Equi-ReSample	0.03	0.05	0.02	0.02	0.05
EquiCon-ReSample	0.001	0.001	0.001	0.001	0.001
Equi-DPS	0.0001	0.001	0.001	0.001	0.1
<i>ImageNet</i> $256 \times 256$					
EquiCon-PSLD	0.0015	0.05	0.06	0.07	0.001

**PSLD.** We integrate EquiReg into PSLD by simply adding an additional gradient update step using our regularization term (Algorithm 2, Algorithm 3).

In our experiments, we use the official PSLD implementation from Rout et al. [38], running with its default settings to reproduce the baseline results. We note that in our code, we do not square the norm when computing the gradient, aligning with PSLD’s implementation.

---

**Algorithm 2** Equi-PSLD for Image Restoration Tasks

---

**Require:**  $T, \mathbf{y}, \{\eta_t\}_{t=1}^T, \{\gamma_t\}_{t=1}^T, \{\tilde{\sigma}_t\}_{t=1}^T$   
**Require:**  $\mathcal{E}, \mathcal{D}, \mathcal{A}\mathbf{x}_0^*, \mathcal{A}, \mathbf{s}_\theta, T_g$  and  $S_g, \{\lambda_t\}_{t=1}^T$

- 1:  $\mathbf{z}_T \sim \mathcal{N}(\mathbf{0}, \mathbf{I})$
- 2: **for**  $t = T - 1$  **to** 0 **do**
- 3:    $\hat{\mathbf{s}} \leftarrow \mathbf{s}_\theta(\mathbf{z}_t, t)$
- 4:    $\mathbf{z}_{0|t} \leftarrow \frac{1}{\sqrt{\alpha_t}}(\mathbf{z}_t + (1 - \bar{\alpha}_t)\hat{\mathbf{s}})$
- 5:    $\epsilon \sim \mathcal{N}(\mathbf{0}, \mathbf{I})$
- 6:    $\mathbf{z}'_{t-1} \leftarrow \frac{\sqrt{\alpha_t(1-\bar{\alpha}_{t-1})}}{1-\bar{\alpha}_t}\mathbf{z}_t + \frac{\sqrt{\bar{\alpha}_{t-1}\beta_t}}{1-\bar{\alpha}_t}\mathbf{z}_{0|t} + \tilde{\sigma}_t\epsilon$
- 7:    $\mathbf{z}''_{t-1} \leftarrow \mathbf{z}'_{t-1} - \eta_t \nabla_{\mathbf{z}_t} \|\mathbf{y} - \mathcal{A}(\mathcal{D}(\mathbf{z}_{0|t}))\|_2^2$
- 8:    $\mathbf{z}_{t-1} \leftarrow \mathbf{z}''_{t-1} - \gamma_t \nabla_{\mathbf{z}_t} \|\mathbf{z}_{0|t} - \mathcal{E}(\mathcal{A}^T \mathcal{A}\mathbf{x}_0^* + (\mathbf{I} - \mathcal{A}^T \mathcal{A})\mathcal{D}(\mathbf{z}_{0|t}))\|_2^2$
- 9:    $\mathbf{z}_{t-1} \leftarrow \mathbf{z}_{t-1} - \lambda_t \nabla_{\mathbf{z}_t} \|S_g(\mathcal{D}(\mathbf{z}_{0|t})) - \mathcal{D}(T_g(\mathbf{z}_{0|t}))\|_2^2$
- 10: **end for**
- 11: **return**  $\mathcal{D}(\mathbf{z}_{0|t})$

---

---

**Algorithm 3** EquiCon-PSLD for Image Restoration Tasks

---

**Require:**  $T, \mathbf{y}, \{\eta_t\}_{t=1}^T, \{\gamma_t\}_{t=1}^T, \{\tilde{\sigma}_t\}_{t=1}^T$   
**Require:**  $\mathcal{E}, \mathcal{D}, \mathcal{A}\mathbf{x}_0^*, \mathcal{A}, \mathbf{s}_\theta, T_g$  and  $S_g, \{\lambda_t\}_{t=1}^T$

- 1:  $\mathbf{z}_T \sim \mathcal{N}(\mathbf{0}, \mathbf{I})$
- 2: **for**  $t = T - 1$  **to** 0 **do**
- 3:    $\hat{\mathbf{s}} \leftarrow \mathbf{s}_\theta(\mathbf{z}_t, t)$
- 4:    $\mathbf{z}_{0|t} \leftarrow \frac{1}{\sqrt{\bar{\alpha}_t}}(\mathbf{z}_t + (1 - \bar{\alpha}_t)\hat{\mathbf{s}})$
- 5:    $\epsilon \sim \mathcal{N}(\mathbf{0}, \mathbf{I})$
- 6:    $\mathbf{z}'_{t-1} \leftarrow \frac{\sqrt{\bar{\alpha}_t(1-\bar{\alpha}_{t-1})}}{1-\bar{\alpha}_t}\mathbf{z}_t + \frac{\sqrt{\bar{\alpha}_{t-1}\beta_t}}{1-\bar{\alpha}_t}\mathbf{z}_{0|t} + \tilde{\sigma}_t\epsilon$
- 7:    $\mathbf{z}''_{t-1} \leftarrow \mathbf{z}'_{t-1} - \eta_t \nabla_{\mathbf{z}_t} \|\mathbf{y} - \mathcal{A}(\mathcal{D}(\mathbf{z}_{0|t}))\|_2^2$
- 8:    $\mathbf{z}_{t-1} \leftarrow \mathbf{z}''_{t-1} - \gamma_t \nabla_{\mathbf{z}_t} \|\mathbf{z}_{0|t} - \mathcal{E}(\mathcal{A}^T \mathcal{A}\mathbf{x}_0^* + (\mathbf{I} - \mathcal{A}^T \mathcal{A})\mathcal{D}(\mathbf{z}_{0|t}))\|_2^2$
- 9:    $\mathbf{z}_{t-1} \leftarrow \mathbf{z}_{t-1} - \lambda_t \nabla_{\mathbf{z}_t} \|\mathbf{z}_{0|t} - \mathcal{E}(S_g^{-1}(\mathcal{D}(T_g(\mathbf{z}_{0|t}))))\|_2^2$
- 10: **end for**
- 11: **return**  $\mathcal{D}(\mathbf{z}_{0|0})$

---

**ReSample.** We integrate EquiReg into ReSample by adding our regularization term into the hard data consistency step (Algorithm 4, Algorithm 5). We note that the ReSample algorithm employs a two-stage approach; initially, it performs pixel-space optimization, and later it performs latent-space optimization. We apply EquiReg in the latent-space optimization stage.

In our experiments, we use the official ReSample implementation from Song et al. [37], running with its default settings to reproduce the baseline results.

---

**Algorithm 4** Equi-ReSample for Image Restoration Tasks

---

**Require:** Measurements  $\mathbf{y}$ ,  $\mathcal{A}(\cdot)$ , Encoder  $\mathcal{E}(\cdot)$ , Decoder  $\mathcal{D}(\cdot)$ , Score function  $\mathbf{s}_\theta(\cdot, t)$ , Pretrained LDM Parameters  $\beta_t, \bar{\alpha}_t, \eta, \delta$ , Hyperparameter  $\gamma$  to control  $\sigma_t^2$ , Time steps to perform resample  $C$ ,  $T_g$  and  $S_g, \{\lambda_t\}_{t=1}^T$

- 1:  $\mathbf{z}_T \sim \mathcal{N}(\mathbf{0}, \mathbf{I})$  ▷ Initial noise vector
- 2: **for**  $t = T - 1, \dots, 0$  **do**
- 3:    $\epsilon_1 \sim \mathcal{N}(\mathbf{0}, \mathbf{I})$
- 4:    $\hat{\epsilon}_{t+1} = \mathbf{s}_\theta(\mathbf{z}_{t+1}, t + 1)$  ▷ Compute the score
- 5:    $\hat{\mathbf{z}}_0(\mathbf{z}_{t+1}) = \frac{1}{\sqrt{\bar{\alpha}_{t+1}}}(\mathbf{z}_{t+1} - \sqrt{1 - \bar{\alpha}_{t+1}}\hat{\epsilon}_{t+1})$  ▷ Predict  $\hat{\mathbf{z}}_0$  using Tweedie's formula
- 6:    $\mathbf{z}'_t = \sqrt{\bar{\alpha}_t}\hat{\mathbf{z}}_0(\mathbf{z}_{t+1}) + \sqrt{1 - \bar{\alpha}_t - \eta\delta^2}\hat{\epsilon}_{t+1} + \eta\delta\epsilon_1$  ▷ Unconditional DDIM step
- 7:   **if**  $t \in C$  **then** ▷ ReSample time step
- 8:     Initialize  $\hat{\mathbf{z}}_0(\mathbf{y})$  with  $\hat{\mathbf{z}}_0(\mathbf{z}_{t+1})$
- 9:     **for each step in gradient descent do**
- 10:        $\mathbf{g} \leftarrow \nabla_{\hat{\mathbf{z}}_0(\mathbf{y})} \frac{1}{2} \|\mathbf{y} - \mathcal{A}(\mathcal{D}(\hat{\mathbf{z}}_0(\mathbf{y})))\|_2^2 + \lambda_t \nabla_{\hat{\mathbf{z}}_0(\mathbf{y})} \|S_g(\mathcal{D}(\hat{\mathbf{z}}_0(\mathbf{y}))) - \mathcal{D}(T_g(\hat{\mathbf{z}}_0(\mathbf{y})))\|_2^2$
- 11:       Update  $\hat{\mathbf{z}}_0(\mathbf{y})$  using gradient  $\mathbf{g}$
- 12:     **end for**
- 13:      $\mathbf{z}_t = \text{StochasticResample}(\hat{\mathbf{z}}_0(\mathbf{y}), \mathbf{z}'_t, \gamma)$  ▷ Map back to  $t$
- 14:   **else**
- 15:      $\mathbf{z}_t = \mathbf{z}'_t$  ▷ Unconditional sampling if not resampling
- 16:   **end if**
- 17: **end for**
- 18:  $\mathbf{x}_0 = \mathcal{D}(\mathbf{z}_0)$  ▷ Output reconstructed image
- 19: **return**  $\mathbf{x}_0$

---



---

**Algorithm 5** EquiCon-ReSample for Image Restoration Tasks

---

**Require:** Measurements  $\mathbf{y}$ ,  $\mathcal{A}(\cdot)$ , Encoder  $\mathcal{E}(\cdot)$ , Decoder  $\mathcal{D}(\cdot)$ , Score function  $s_\theta(\cdot, t)$ , Pretrained LDM Parameters  $\beta_t$ ,  $\bar{\alpha}_t$ ,  $\eta$ ,  $\delta$ , Hyperparameter  $\gamma$  to control  $\sigma_t^2$ , Time steps to perform resample  $C$ ,  $T_g$  and  $S_g$ ,  $\{\lambda_t\}_{t=1}^T$

- 1:  $\mathbf{z}_T \sim \mathcal{N}(\mathbf{0}, \mathbf{I})$  ▷ Initial noise vector
- 2: **for**  $t = T - 1, \dots, 0$  **do**
- 3:    $\epsilon_1 \sim \mathcal{N}(\mathbf{0}, \mathbf{I})$
- 4:    $\hat{\epsilon}_{t+1} = s_\theta(\mathbf{z}_{t+1}, t + 1)$  ▷ Compute the score
- 5:    $\hat{\mathbf{z}}_0(\mathbf{z}_{t+1}) = \frac{1}{\sqrt{\bar{\alpha}_{t+1}}}(\mathbf{z}_{t+1} - \sqrt{1 - \bar{\alpha}_{t+1}}\hat{\epsilon}_{t+1})$  ▷ Predict  $\hat{\mathbf{z}}_0$  using Tweedie's formula
- 6:    $\mathbf{z}'_t = \sqrt{\bar{\alpha}_t}\hat{\mathbf{z}}_0(\mathbf{z}_{t+1}) + \sqrt{1 - \bar{\alpha}_t - \eta\delta^2}\hat{\epsilon}_{t+1} + \eta\delta\epsilon_1$  ▷ Unconditional DDIM step
- 7:   **if**  $t \in C$  **then** ▷ ReSample time step
- 8:     Initialize  $\hat{\mathbf{z}}_0(\mathbf{y})$  with  $\hat{\mathbf{z}}_0(\mathbf{z}_{t+1})$
- 9:     **for each step in gradient descent do**
- 10:        $\mathbf{g} \leftarrow \nabla_{\hat{\mathbf{z}}_0(\mathbf{y})} \frac{1}{2} \|\mathbf{y} - \mathcal{A}(\mathcal{D}(\hat{\mathbf{z}}_0(\mathbf{y})))\|_2^2 + \lambda_t \nabla_{\hat{\mathbf{z}}_0(\mathbf{y})} \|\hat{\mathbf{z}}_0(\mathbf{y}) - \mathcal{E}(S_g^{-1}(\mathcal{D}(T_g(\hat{\mathbf{z}}_0(\mathbf{y}))))\|_2^2$
- 11:       Update  $\hat{\mathbf{z}}_0(\mathbf{y})$  using gradient  $\mathbf{g}$
- 12:     **end for**
- 13:      $\mathbf{z}_t = \text{StochasticResample}(\hat{\mathbf{z}}_0(\mathbf{y}), \mathbf{z}'_t, \gamma)$  ▷ Map back to  $t$
- 14:   **else**
- 15:      $\mathbf{z}_t = \mathbf{z}'_t$  ▷ Unconditional sampling if not resampling
- 16:   **end if**
- 17: **end for**
- 18:  $\mathbf{x}_0 = \mathcal{D}(\mathbf{z}_0)$  ▷ Output reconstructed image
- 19: **return**  $\mathbf{x}_0$

---

**DPS.** Similar to PSLD, we integrate EquiReg into DPS by simply adding an additional gradient update step using our regularization term (Algorithm 6).

In our experiments, we use the official DPS implementation from Chung et al. [32], running with its default settings to reproduce the baseline results.

---

**Algorithm 6** Equi-DPS for Image Restoration Tasks

---

**Require:**  $T, \mathbf{y}, \{\zeta_t\}_{t=1}^T, \{\tilde{\sigma}_t\}_{t=1}^T, s_\theta, \mathcal{E}, T_g$  and  $S_g, \{\lambda_t\}_{t=1}^T$

- 1:  $\mathbf{x}_T \sim \mathcal{N}(\mathbf{0}, \mathbf{I})$
- 2: **for**  $t = T - 1$  **to** 0 **do**
- 3:    $\hat{\mathbf{s}} \leftarrow s_\theta(\mathbf{x}_t, t)$
- 4:    $\mathbf{x}_{0|t} \leftarrow \frac{1}{\sqrt{\bar{\alpha}_t}}(\mathbf{x}_t + (1 - \bar{\alpha}_t)\hat{\mathbf{s}})$
- 5:    $\epsilon \sim \mathcal{N}(\mathbf{0}, \mathbf{I})$
- 6:    $\mathbf{x}'_{t-1} \leftarrow \frac{\sqrt{\bar{\alpha}_t}(1 - \bar{\alpha}_{t-1})}{1 - \bar{\alpha}_t} \mathbf{x}_t + \frac{\sqrt{\bar{\alpha}_{t-1}}\beta_t}{1 - \bar{\alpha}_t} \mathbf{x}_{0|t} + \tilde{\sigma}_t \epsilon$
- 7:    $\mathbf{x}_{t-1} \leftarrow \mathbf{x}'_{t-1} - \zeta_t \nabla_{\mathbf{x}_t} \|\mathbf{y} - \mathcal{A}(\mathbf{x}_{0|t})\|_2^2$
- 8:    $\mathbf{x}_{t-1} \leftarrow \mathbf{x}_{t-1} - \lambda_t \nabla_{\mathbf{x}_t} \|S_g(\mathcal{E}(\mathbf{x}_{0|t})) - \mathcal{E}(T_g(\mathbf{x}_{0|t}))\|_2^2$
- 9: **end for**
- 10: **return**  $\mathbf{x}_0$

---

**LatentDAPS.** We integrate EquiReg into LatentDAPS by simply adding an additional gradient update step using our regularization term (Algorithm 7).

In our experiments, we use the official LatentDAPS implementation from Zhang et al. [40], running with its default settings to reproduce the baseline results.

---

**Algorithm 7** Equi-LatentDAPS for Image Restoration Tasks

---

**Require:** Latent space score model  $s_\theta$ , measurement  $\mathbf{y}$ , noise schedule  $\sigma_t$ ,  $\{t_i\}_{i \in \{0, \dots, N_A\}}$ , encoder  $\mathcal{E}$  and decoder  $\mathcal{D}$ ,  $T_g$  and  $S_g$ ,  $\{\lambda_t\}_{t=1}^T$

- 1: Sample  $\mathbf{z}_T \sim \mathcal{N}(\mathbf{0}, \sigma_T^2 \mathbf{I})$
- 2: **for**  $i = N_A, N_A - 1, \dots, 1$  **do**
- 3:   Compute  $\hat{\mathbf{z}}_0^{(0)} = \hat{\mathbf{z}}_0(\mathbf{z}_{t_i})$  by solving the probability flow ODE with  $s_\theta$
- 4:   **for**  $j = 0, \dots, N - 1$  **do**
- 5:      $\mathbf{g} \leftarrow \nabla_{\hat{\mathbf{z}}_0} \log p(\hat{\mathbf{z}}_0^{(j)} | \mathbf{z}_{t_i}) + \nabla_{\hat{\mathbf{z}}_0} \log p(\mathbf{y} | \hat{\mathbf{z}}_0^{(j)}) + \lambda_t \nabla_{\hat{\mathbf{z}}_0} \|S_g(\mathcal{D}(\hat{\mathbf{z}}_0^{(j)})) - \mathcal{D}(T_g(\hat{\mathbf{z}}_0^{(j)}))\|_2^2$
- 6:      $\hat{\mathbf{z}}_0^{(j+1)} \leftarrow \hat{\mathbf{z}}_0^{(j)} + \eta_t \mathbf{g} + \sqrt{2\eta_t} \epsilon_j$ ,  $\epsilon_j \sim \mathcal{N}(\mathbf{0}, \mathbf{I})$
- 7:   **end for**
- 8:   Sample  $\mathbf{z}_{t_{i-1}} \sim \mathcal{N}(\hat{\mathbf{z}}_0^{(N)}, \sigma_{t_{i-1}}^2 \mathbf{I})$
- 9: **end for**
- 10: **return**  $\mathcal{D}(\mathbf{z}_0)$

---

## F Experiment Setup for PDE Reconstructions

**Helmholtz equation.** The Helmholtz equation represents wave propagation in heterogeneous media:

$$\nabla^2 u(x) + k^2 u(x) = a(x), \quad x \in (0, 1)^2, \quad (7)$$

with  $k = 1$  and  $u|_{\partial\Omega} = 0$ . Coefficient fields  $a(x)$  are generated according to  $a \sim \mathcal{N}(0, (-\Delta + 9\mathbf{I})^2)$ . We note that this system has reflection equivariance along  $x_1 = \frac{1}{2}, x_2 = \frac{1}{2}, x_1 = x_2$  and rotation equivariance by  $\frac{\pi}{2}, \pi, \frac{3\pi}{2}$ .

**Navier-Stokes equations.** Following the methodology of [135], we model the time evolution of a vorticity field,  $u(x, t)$ , governed by:

$$\partial_t u(x, t) + \mathbf{w}(x, t) \cdot \nabla u(x, t) = \nu \Delta u(x, t) + f(x), \quad x \in (0, 1)^2, t \in (0, T], \quad (8)$$

$$\nabla \cdot \mathbf{w}(x, t) = 0, \quad x \in (0, 1)^2, t \in [0, T], \quad (9)$$

$$u(x, 0) = a(x), \quad x \in (0, 1)^2, \quad (10)$$

where  $\mathbf{w}$  is the velocity field;  $\nu = \frac{1}{1000}$ , viscosity; and  $f$ , a fixed forcing term. The initial condition  $a(x)$  is drawn from  $\mathcal{N}(0, 7^{3/2}(-\Delta + 49\mathbf{I})^{-5/2})$  under periodic boundary conditions. The forcing term is  $f(x) = 0.1(\sin(2\pi(x_1 + x_2)) + \cos(2\pi(x_1 + x_2)))$ . We borrow the dataset from [51]. We note that this system has a reflection symmetry along the  $x_1 = x_2$  axis.

**Implementation details.** EquiReg, as a regularizer for diffusion posterior sampling, can be adapted to many inverse solvers in a plug-and-play manner. For PDE experiments, we use the same model weights and configurations as FunDPS [57]. Error rates are calculated using the  $L^2$  relative error between the predicted and true solutions, averaged on 100 randomly selected test samples. We provide the information on the EquiReg scaling weights in Table 9.

Table 9: EquiReg loss used in PDE experiments.

	Helmholtz		Navier-Stokes	
	Forward	Inverse	Forward	Inverse
EquiReg Norm Type	MSE	L2	MSE	L2
EquiReg Weight $\lambda$	100	100	100	1000

## G Theoretical Analysis

In this section, we provide the proofs for [Proposition 4.1](#) and [Proposition 4.2](#).

### G.1 Preliminary and Notations

We first remind the readers of gradient flow under the Wasserstein-2 metric and introduce the notations related to the diffusion model.

**Wasserstein Gradient Flow** Let  $\mathcal{F} : \mathcal{P}_2(\mathbb{R}^d) \rightarrow \mathbb{R} \cup \{+\infty\}$  be a functional of probability distributions. The Wasserstein gradient flow of  $\mathcal{F}$  is characterized by the minimizing movement scheme (also known as JKO scheme) introduced by [\[136\]](#). For a fixed time step  $\tau > 0$ , the sequence  $(\rho_k)_{k \in \mathbb{N}}$  of probability densities is defined recursively by:

$$\rho_{k+1} \in \arg \min_{\rho \in \mathcal{P}_2(\mathbb{R}^d)} \left\{ \frac{1}{2\tau} W_2^2(\rho, \rho_k) + \mathcal{F}(\rho) \right\},$$

where  $W_2$  denotes the 2-Wasserstein distance, and each  $\rho_k$  is a probability density representing the distribution at time  $t = k\tau$ . In the limit  $\tau \rightarrow 0$ , this discrete-time scheme recovers the continuous-time gradient flow of  $\mathcal{F}$  under the  $W_2$  metric.

**Diffusion Model** A diffusion model defines a forward stochastic process  $(\mathbf{x}_t)_{t \in [0, T]}$  governed by the Itô SDE:

$$d\mathbf{x}_t = f(\mathbf{x}_t, t) dt + \sqrt{\beta_t} d\mathbf{w}_t, \quad (11)$$

where  $\mathbf{w}_t$  is standard Brownian motion,  $\beta_t > 0$  is a time-dependent variance schedule, and  $f(\mathbf{x}, t)$  is a drift term. For instance,  $f \equiv 0$  for a variance-exploding SDE and  $f(\mathbf{x}, t) = -\frac{\beta_t}{2} \mathbf{x}$  for a variance-preserving SDE defined in [\[30\]](#). In this work, we carry out our analysis under a more general setting.

**Assumption G.1.** *The drift term is a gradient field,  $f(\mathbf{x}, t) = \nabla h(\mathbf{x}, t)$  for a scalar function  $h$ .*

This process progressively transforms an initial data distribution  $\mathbf{x}_0 \sim p_0$  into a tractable reference distribution (e.g., approximately a Gaussian  $\mathcal{N}(0, I)$ ) at time  $T$ .

Sampling is performed by simulating the *reverse-time SDE*:

$$d\mathbf{x}_t = [f(\mathbf{x}_t, t) - \beta_t \nabla_{\mathbf{x}} \log p_t(\mathbf{x}_t)] dt + \sqrt{\beta_t} d\bar{\mathbf{w}}_t, \quad (12)$$

where  $p_t$  is the marginal density of  $\mathbf{x}_t$ , and  $\bar{\mathbf{w}}_t$  is a standard Brownian motion in reverse time.

In practice, the score function  $\nabla_{\mathbf{x}} \log p_t(\mathbf{x})$  is approximated by a neural network  $s_\theta(\mathbf{x}, t)$  trained to estimate the score of the forward process. For *conditional sampling*, where we sample  $\mathbf{x}_0$  given some observed variable  $\mathbf{y}$ , the score is replaced by  $\nabla_{\mathbf{x}} \log p_t(\mathbf{x}|\mathbf{y})$  and decomposed as

$$\nabla_{\mathbf{x}} \log p_t(\mathbf{x}|\mathbf{y}) = \nabla_{\mathbf{x}} \log p_t(\mathbf{x}) + \nabla_{\mathbf{x}} \log p_t(\mathbf{y}|\mathbf{x}), \quad (13)$$

based on Bayes' rule.

To simplify notation in the sequel, we perform a time reparameterization  $t = T - t'$ , so that the reverse process is written as a forward SDE over  $t \in [0, T]$ :

$$d\mathbf{x}_t = -[f(\mathbf{x}_t, T - t) - \beta_{T-t} [\nabla_{\mathbf{x}} \log p_{T-t}(\mathbf{x}_t) + \nabla_{\mathbf{x}} \log p_t(\mathbf{y}|\mathbf{x}_t)]] dt + \sqrt{\beta_{T-t}} d\mathbf{w}_t, \quad (14)$$

This form describes the generative process as evolving forward from  $t = 0$  to  $t = T$ , matching the usual direction of analysis in gradient flow frameworks.

## G.2 Proof of Proposition 4.1

In this work, we consider Wasserstein gradient flow under the setting where the functional  $\mathcal{F}$  depends on time.

**Lemma G.1.** *Consider a time-dependent functional  $\mathcal{F}(\rho, t) = \int \rho(\mathbf{x})V(\mathbf{x}, t)d\mathbf{x} + \int \alpha(t)\rho \log \rho d\mathbf{x}$ . Then the particle description of Wasserstein-2 gradient flow associated with this functional derived by JKO scheme is*

$$d\mathbf{x}_t = -\nabla V(\mathbf{x}_t, t)dt + \sqrt{2\alpha(t)}d\mathbf{w}_t. \quad (15)$$

*Proof.* Consider the following optimization

$$\min_{\rho'} \mathcal{F}(\rho', t + \Delta t) - \mathcal{F}(\rho, t) + \frac{1}{2\Delta t} W_2^2(\rho, \rho'), \quad (16)$$

where the change of density is restricted to the Liouville equation

$$\partial_t \rho = -\nabla \cdot (\rho v(\mathbf{x}, t)), \text{ and } \rho'(\mathbf{x}) = \rho(\mathbf{x}) - \Delta t \nabla \cdot (\rho(\mathbf{x})v(\mathbf{x})) + o(\Delta t). \quad (17)$$

Using the static formulation of  $W_2$  distance, we have

$$W_2^2(\rho, \rho') = \int \rho(\mathbf{x}) \|\mathbf{x} - T^*(\mathbf{x})\|^2 d\mathbf{x} = \Delta t^2 \int \rho(\mathbf{x}) \|v^*(\mathbf{x})\|^2 d\mathbf{x}, \quad (18)$$

where  $T^*(\mathbf{x})$  is the optimal transport map, and  $v^*(\mathbf{x})$  is the associated optimal velocity field.

Thus, we can rewrite the eq. (16) as

$$\inf_v \mathcal{F}(\rho, t) - \Delta t \int \nabla \cdot (\rho(\mathbf{x})v(\mathbf{x})) \frac{\delta \mathcal{F}(\rho, t)}{\delta \rho}(\mathbf{x}) d\mathbf{x} + \Delta t \int [\rho(\mathbf{x})\partial_t V(\mathbf{x}, t) + \dot{\alpha}(t)\rho \log \rho] d\mathbf{x} \quad (19)$$

$$- \mathcal{F}(\rho, t) + \frac{\Delta t}{2} \int \rho(\mathbf{x}) \|v(\mathbf{x})\|^2 d\mathbf{x}, \quad (20)$$

which simplifies to

$$\min_v \int \rho(\mathbf{x}) \left\langle v(\mathbf{x}), \nabla \frac{\delta \mathcal{F}(\rho, t)}{\delta \rho}(\mathbf{x}) \right\rangle d\mathbf{x} + \frac{1}{2} \int \rho(\mathbf{x}) \|v(\mathbf{x})\|^2 d\mathbf{x}, \quad (21)$$

since the last term in the first line of (19) does not depend on  $v$ . and further to

$$\min_v \int \rho(\mathbf{x}) \left\| v(\mathbf{x}) + \nabla \frac{\delta \mathcal{F}(\rho, t)}{\delta \rho}(\mathbf{x}) \right\|^2 d\mathbf{x}. \quad (22)$$

From the optimality condition of the above problem, we obtain

$$v(\mathbf{x}, t) = -\nabla \frac{\delta \mathcal{F}(\rho, t)}{\delta \rho}(\mathbf{x}) = -(\nabla V(\mathbf{x}, t) + \alpha(t)\nabla \log \rho(\mathbf{x}, t)). \quad (23)$$

The corresponding evolution of probability density is

$$\partial_t \rho(\mathbf{x}, t) = -\nabla \cdot (\rho(\mathbf{x}, t)v(\mathbf{x}, t)) \quad (24)$$

$$= \nabla \cdot (\rho(\mathbf{x}, t)(\nabla V(\mathbf{x}, t) + \alpha(t)\frac{\nabla \rho(\mathbf{x}, t)}{\rho})) \quad (25)$$

$$= -\nabla \cdot (\rho(\mathbf{x}, t)(-\nabla V(\mathbf{x}, t)) + \alpha(t)\Delta \rho(\mathbf{x}, t)), \quad (26)$$

which is exactly the Fokker-Planck equation describing the evolution of the probability density describing the particles following

$$d\mathbf{x}_t = -\nabla V(\mathbf{x}_t, t)dt + \sqrt{2\alpha(t)}d\mathbf{w}_t. \quad (27)$$

□

Now we come back to Proposition 4.1. From eq. (14) we know that choosing

$$V(\mathbf{x}, t) = h(\mathbf{x}, T - t) - \beta_{T-t}[\log p_{T-t}(\mathbf{x}) + \log p_{T-t}(\mathbf{y}|\mathbf{x})] \text{ and } \alpha(t) = \frac{\beta_{T-t}}{2} \quad (28)$$

in Lemma G.1 completes the proof, where  $h$  is defined in Assumption G.1.

### G.3 Detailed version of Proposition 4.2

In practice, one does not have access to  $\log p_t(\mathbf{y}|\mathbf{x}_t)$  which appears in the reverse SDE. The most popular approach is to do the following approximation,

$$p_t(\mathbf{y}|\mathbf{x}_t) = \int p(\mathbf{y}|\mathbf{x}_0)p(\mathbf{x}_0|\mathbf{x}_t)d\mathbf{x}_0 = \mathbb{E}_{\mathbf{x}_0 \sim p(\mathbf{x}_0|\mathbf{x}_t)}[p(\mathbf{y}|\mathbf{x}_0)] \approx p(\mathbf{y}|\mathbb{E}[\mathbf{x}_0|\mathbf{x}_t]), \quad (29)$$

which can be interpreted as exchanging two operations, the conditional expectation and the measurement  $p(\mathbf{y}|\cdot)$ .

As discussed in the main text, since the conditional expectation is a linear combination over all possible values of  $\mathbf{x}_0$ , it may fall outside the data manifold, resulting in physically invalid samples. One of the central challenges in diffusion-based inverse sampling is guiding the sampling trajectory—generated by the reverse SDE dynamics—toward the data manifold. A common strategy is to incorporate regularization into the reverse SDE to encourage manifold adherence. In this work, building on the perspective of Wasserstein gradient flow as outlined above, we provide a novel interpretation of the role played by such regularization terms.

We show that the regularizer serves to reweight the contribution of different regions in the calculation of the underlying functional being minimized,  $\Phi(\rho, t)$  defined in Proposition 4.1. Specifically, it amplifies the influence of regions where the density estimate is reliable (typically near the data manifold), while down-weighting regions with poor approximation quality of based on eq. (29), often corresponding to off-manifold samples.

Following from what we have shown in the main text,  $\Phi(\rho, t)$  has the form of  $\beta_{T-t} \int [\rho\phi(\mathbf{x}, t) + \frac{1}{2}\rho \log \rho]d\mathbf{x}$  for a function  $\phi(\mathbf{x}, t)$ , which can be derived by (28). The  $\log p_t(\mathbf{y}|\mathbf{x})$  term in (28) or  $\nabla \log p_t(\mathbf{y}|\mathbf{x})$  term in (27), equivalently, is computed based on approximation (29). We denote the corresponding approximation of  $\phi(\mathbf{x}, t)$  as  $\hat{\phi}(\mathbf{x}, t)$ . As discussed in the main text, we can assume without loss of generality that  $\phi(\mathbf{x}, t) < 0$  and  $\hat{\phi}(\mathbf{x}, t) < 0$ . We have

$$\hat{\Phi}(\rho, t) = \beta_{T-t} \left[ \int_{\mathbf{x} \in N(\mathcal{M})} \rho(\mathbf{x}) \hat{\phi}(\mathbf{x}, t) d\mathbf{x} + \int_{\mathbf{x} \notin N(\mathcal{M})} \rho(\mathbf{x}) \hat{\phi}(\mathbf{x}, t) d\mathbf{x} + \frac{1}{2} \int \rho \log \rho d\mathbf{x} \right], \quad (30)$$

where  $N(\mathcal{M})$  denotes a neighborhood of the data manifold  $\mathcal{M}$ . Intuitively, we aim to focus on the contribution from regions near  $\mathcal{M}$ , which corresponds to the first term, while down-weighting the influence of points farther away, where the approximation tends to be unreliable. For instance, we can introduce two positive weights  $A \gg B$  and adopt the modified functional

$$\tilde{\Phi}(\rho, t) = \beta_{T-t} \left[ A \int_{\mathbf{x} \in N(\mathcal{M})} \rho(\mathbf{x}) \hat{\phi}(\mathbf{x}, t) d\mathbf{x} + B \int_{\mathbf{x} \notin N(\mathcal{M})} \rho(\mathbf{x}) \hat{\phi}(\mathbf{x}, t) d\mathbf{x} + \frac{1}{2} \int \rho \log \rho d\mathbf{x} \right]. \quad (31)$$

In this work, we further generalize this idea and consider a continuous weight function,

$$\tilde{\Phi}(\rho, t) = \beta_{T-t} \left[ \int \rho(\mathbf{x}) \hat{\phi}(\mathbf{x}, t) \lambda(\mathbf{x}) d\mathbf{x} + \frac{1}{2} \int \rho \log \rho d\mathbf{x} \right], \quad (32)$$

where the non-negative weight  $\lambda(\mathbf{x})$  is large for  $\mathbf{x} \in N(\mathcal{M})$  and small elsewhere.

In practice, a nonnegative regularization function  $\mathcal{R}(\mathbf{x})$  is introduced, ideally being nearly zero for  $\mathbf{x}$  near the data manifold and much larger elsewhere. We consider the following modified functional with weight function  $\lambda(\mathbf{x}, t) := e^{\frac{\mathcal{R}(\mathbf{x})}{\hat{\phi}(\mathbf{x}, t)}}$ ,

$$\tilde{\Phi}(\rho, t) = \beta_{T-t} \left[ \int \rho(\mathbf{x}) \hat{\phi}(\mathbf{x}, t) e^{\frac{\mathcal{R}(\mathbf{x})}{\hat{\phi}(\mathbf{x}, t)}} d\mathbf{x} + \frac{1}{2} \int \rho(\mathbf{x}) \log \rho(\mathbf{x}) d\mathbf{x} \right]. \quad (33)$$

Note that  $\hat{\phi} < 0$ , we have that

$$\mathcal{R}(\mathbf{x}) \approx \begin{cases} 0, & \mathbf{x} \in N(\mathcal{M}) \\ \gg 1, & \mathbf{x} \text{ far away from } N(\mathcal{M}) \end{cases} \Rightarrow \lambda(\mathbf{x}, t) \approx \begin{cases} 1, & \mathbf{x} \in N(\mathcal{M}) \\ 0, & \mathbf{x} \text{ far away from } N(\mathcal{M}) \end{cases}.$$

Next, we consider practical algorithms based on this reweighted functional. In practice, we only have the score function instead of the function value of  $\log p_{T-t}(\mathbf{x})$ . Thus, the Wasserstein gradient flow associated with



(33) is intractable since we cannot evaluate the weight function. We consider the following approximation based on  $e^\delta \approx 1 + \delta$ ,

$$\tilde{\Phi}(\rho, t) \approx \beta_{T-t} \left[ \int \rho(\mathbf{x}) \hat{\phi}(\mathbf{x}, t) \left( 1 + \frac{\mathcal{R}(\mathbf{x})}{\hat{\phi}(\mathbf{x}, t)} \right) d\mathbf{x} + \frac{1}{2} \int \rho(\mathbf{x}) \log \rho(\mathbf{x}) d\mathbf{x} \right] \quad (34)$$

$$= \beta_{T-t} \left[ \int \rho(\mathbf{x}) (\hat{\phi}(\mathbf{x}, t) + \mathcal{R}(\mathbf{x})) d\mathbf{x} + \frac{1}{2} \int \rho(\mathbf{x}) \log \rho(\mathbf{x}) d\mathbf{x} \right]. \quad (35)$$

By Lemma G.1, the dynamics of  $\mathbf{x}$  driven by the Wasserstein gradient flow associated with the approximated functional above is

$$d\mathbf{x} = [-f(\mathbf{x}, T-t) - \beta_{T-t} \nabla_{\mathbf{x}} (\log p_{T-t}(\mathbf{x}) + \log \hat{p}_{T-t}(\mathbf{y}|\mathbf{x}) + \mathcal{R}(\mathbf{x}))] dt + \sqrt{\beta_{T-t}} d\bar{\mathbf{w}}. \quad (36)$$

This completes the proof.

**Remark 1.** Since  $\hat{\phi} < 0$ , and  $e^A \geq 1 + A$  for any  $A \in \mathbb{R}$ , the dynamics derived by the approximated functional in (35) is evolving to minimize an upper bound of the reweighted functional  $\tilde{\Phi}$ .

## H Additional Background Information

**Solving inverse problems with deep learning prior to diffusion models.** Earlier works [137–140] used deep neural networks as denoisers to solve inverse problems. Furthermore, deep generative models such as variational autoencoders (VAEs) [141], and generative adversarial networks (GANs) [142] were employed. Notable applications include compressed sensing [143] and MRI [144].

**Resources for Definition 4.2 on vanishing-error autoencoders.** Manifold constrained distribution-dependent equivariance error uses the notion of *vanishing-error autoencoders* [145, 146, 62] (Definition H.1), also known as an asymptotically-trained autoencoder [146] or a perfect autoencoder [62]. Vanishing-error autoencoders have previously been employed by diffusion-based inverse solvers to preserve the diffusion process on the manifold [62].

**Definition H.1** (Vanishing-Error Autoencoder). *A vanishing-error autoencoder under the manifold  $\mathcal{M}$  with encoder  $\mathcal{E} : \mathcal{X} \rightarrow \mathcal{Z}$  and decoder  $\mathcal{D} : \mathcal{Z} \rightarrow \mathcal{X}$  with  $\mathcal{Z} = \mathbb{R}^k$  where  $k < d$ , has zero reconstruction error under the support of the data distribution  $\mathcal{X}$ , i.e.,  $\forall \mathbf{x} \in \mathcal{X} \subset \mathcal{M}$ ,  $\mathbf{x} = \mathcal{D}(\mathcal{E}(\mathbf{x}))$ . It follows that the decoder is surjective on the data manifold,  $\mathcal{D} : \mathcal{Z} \rightarrow \mathcal{M}$  [62], and the encoder-decoder composition forms an identity map, i.e.,  $\forall \mathbf{z} \in \mathcal{M}$ ,  $\mathbf{z} = \mathcal{E}(\mathcal{D}(\mathbf{z}))$ .*

**Equivariance.** Let  $\mathbf{z} \in \mathbb{R}^d$  and  $\mathbf{x} = f(\mathbf{z}) \in \mathbb{R}^d$ . For rotation and reflection equivariance, the transformations  $T_g$  and  $S_g$  can be defined by a rotation matrix  $\mathbf{R} \in \mathbb{R}^{d \times d}$ ; then, a function  $f$  with the rotation equivariant property would satisfy  $\mathbf{R}\mathbf{x} = f(\mathbf{R}\mathbf{z})$ . For translation equivariance, the transformations would be  $T_g(\mathbf{z}) = \mathbf{z} + g$  and  $S_g(\mathbf{x}) = \mathbf{x} + g$ , where  $g \in \mathbb{R}^d$ . Hence, for a translation equivariance function  $f$ , we would have  $\mathbf{x} + g = f(\mathbf{z} + g)$ . For the case where the output dimension is larger than the input,  $f : \mathbb{R}^k \rightarrow \mathbb{R}^d$  with  $d > k$ , translation equivariance can be defined up to a discrete scale, i.e.,  $T_g(\mathbf{z}) = \mathbf{z} + g$  and  $S_g(\mathbf{x}) = T_{sg}(\mathbf{z})$  where  $s = d/k$ . The equivariance properties of translation, rotation, and reflections, combined, are referred to as E(3) symmetries. Without reflections, the symmetries form a Euclidean group SE(3) [112, 113].

## I Computing Resources

We conduct experiments on two NVIDIA GeForce RTX 4090 GPUs with 24 GB of VRAM. We note that we use pre-trained models and perform inference, so not much compute is required.

## **J Assets**

We use the publicly available code from PSLD (<https://github.com/LituRout/PSLD>), ReSample (<https://github.com/soominkwon/resample>), DPS (<https://github.com/DPS2022/diffusion-posterior-sampling>), and LatentDAPS (<https://github.com/zhangbingliang2019/DAPS>).

## **K Broader Impacts**

On the positive side, high-fidelity image restoration can improve downstream tasks in medical imaging, remote-sensing and environmental monitoring (e.g., denoising satellite observations to track pollution or deforestation). Likewise, accelerated PDE-solving via learned diffusion priors may enable faster, more accurate simulations for climate modeling, fluid-dynamics research, and engineering design. On the other hand, robust reconstruction methods could be misappropriated for privacy-invasive surveillance or to create deceptive imagery. We emphasize that our method does not amplify these existing risks.

## **L Responsible Release**

Our approach uses only publicly available datasets and standard pre-trained diffusion models, introducing no novel dual-use or privacy risks. Consequently, no additional safeguards are required.